

Changes in Stratospheric Climate and Age-of-Air in Recent GEOS Systems since MERRA-2

Clara Orbe^{1,2}, Lawrence L. Takacs^{3,4}, Amal El Akkraoui³,
Krzysztof Wargan^{3,4}, Andrea Molod³, William Putman³, Steven Pawson³

¹NASA Goddard Institute for Space Studies, New York, NY

²Department of Applied Physics and Applied Mathematics, Columbia University, New York, NY

³Global Modeling and Assimilation Office, NASA Goddard Space Flight Center, Greenbelt, MD

⁴Science Systems and Applications, Inc., Lanham, MD, USA

Key Points:

- The stratospheric mean age-of-air simulated in GEOS is sensitive to the remapping scheme used within the finite-volume dynamical core.
- This sensitivity in the age-of-air is significant ($\sim 30\%$) and imprints on the simulated distributions of several long-lived chemical trace gases, including nitrous oxide and methane.
- The age-of-air sensitivities primarily reflect changes in resolved wave convergence over the Northern Hemisphere midlatitude stratosphere, which impact mean upwelling in the tropical lower stratosphere.

Corresponding author: Clara Orbe, clara.orbe@nasa.gov

18 **Abstract**

19 Accurately modeling the large-scale transport of trace gases and aerosols is critical for interpreting past (and projecting future) changes in atmospheric composition. Simulations of the stratospheric mean age-of-air continue to show persistent biases in chemistry climate models, although the drivers of these biases are not well understood. Here we identify one driver of simulated stratospheric transport differences among various NASA Global Earth Observing System (GEOS) candidate model versions under consideration for the upcoming GEOS Retrospective analysis for the 21st Century (GEOS-R21C). In particular, we show that the simulated age-of-air values are sensitive to the so-called “remapping” algorithm used within the finite-volume dynamical core, which controls how individual material surfaces are vertically interpolated back to standard pressure levels after each horizontal advection time step. Differences in the age-of-air resulting from changes within the remapping algorithm approach ~ 1 year over the high latitude middle stratosphere – or about 30% climatological mean values – and imprint on several trace gases, including methane (CH_4) and nitrous oxide (N_2O). These transport sensitivities reflect, to first order, changes in the strength of tropical upwelling in the lower stratosphere (70–100 hPa) which are driven by changes in resolved wave convergence over northern mid-latitudes as (critical lines of) wave propagation shift in latitude. Our results strongly support continued examination of the role of numerics in contributing to transport biases in composition modeling.

38 **Plain Language Summary**

39 Large-scale transport plays a crucial role in distributing climatically important trace constituents in the atmosphere, especially in the stratosphere where transport largely determines the chemical lifetimes of trace gases. One summary of transport in the stratosphere is the “mean age” or the mean transit time since air at a point in the stratosphere was last in the troposphere. Current models used for simulating stratospheric composition produce a range of simulated ages, although these differences are poorly understood. Among other factors, model numerics play a critical role in transport, but few studies have explored the sensitivity of the mean age to the choice of numerical scheme employed within different dynamical cores. Here we use one model to show that the mean age is sensitive to the so-called “remapping” algorithm used within the finite-volume dynamical core that controls how individual material surfaces are vertically interpolated back to standard pressure levels after each horizontal advection time step. This reflects sensitivities in the representation of how waves propagate from the troposphere into the stratosphere. This work suggests that model numerics can be an important factor in contributing to differences in simulated transport among models.

54 **1 Introduction**

55 The chemical and radiative properties of the troposphere and lower stratosphere are strongly influenced by the stratosphere-troposphere exchange of mass and tracers (e.g., Morgenstern and Carver (2001); Hegglin et al. (2006); Pan et al. (2007)). Properly simulating the stratospheric circulation and its influence on atmospheric composition in earth system models is important for capturing past decadal trends in surface climate, particularly in response to changes in Southern Hemisphere ozone depletion (e.g., Son et al. (2009); Polvani et al. (2011)). In the Northern Hemisphere (NH), the stratospheric circulation’s coupling to ozone could represent an important feedback on the climate’s response to future increases in greenhouse gases (GHGs), especially over the North Atlantic (e.g., Chiodo and Polvani (2019)). On shorter subseasonal timescales, stratospheric ozone changes associated with strong polar vortex states may also modulate Arctic sea level pressure and surface temperatures (e.g., Ivy et al. (2017); Oehrlein et al. (2020)), so much so that seasonal forecast systems employing prognostic ozone show suggestions

68 of increased signal-to-noise ratio in predictions of the North Atlantic Oscillation (B. M. Monge-
69 Sanz et al. (2022)).

70 Key to accurately simulating a consistent representation of coupling between strato-
71 spheric dynamics and chemical trace gases is ensuring that a model’s underlying trans-
72 port circulation is properly represented. To this end, much effort has been paid to de-
73 veloping and refining so-called “tracer-independent” metrics of transport (Holzer and Hall
74 (2000)) such as the mean age-of-air (Hall and Plumb (1994)) and to applying these mea-
75 sures to rigorously evaluate model transport characteristics in chemistry climate mod-
76 els (CCMs) (e.g., Hall et al. (1999); Orbe et al. (2018); Dietmüller et al. (2018); Aba-
77 los et al. (2020)).

78 While the assessment of CCMs participating in the SPARC Chemistry Climate Model
79 Validation (SPARC CCMVal) effort showed a marked improvement in simulated trans-
80 port characteristics relative to previous intercomparisons (J. Neu et al. (2010)), more re-
81 cent analysis of models participating in the SPARC Chemistry Climate Modeling Ini-
82 tiative (CCMI) (Eyring et al. (2013)) do not demonstrate any improvement (Dietmüller
83 et al. (2018), see their Figure 3). In particular, although some models produce mean age
84 values that agree well with observational estimates, the CCMI intermodel spread is \sim
85 50%, with models generally simulating transport that is too vigorous relative to obser-
86 vations. While documenting these transport differences among models is straightforward,
87 understanding the drivers of this spread remains a challenge and there is still no con-
88 sensus on what is causing the large spread in simulated ages among the current gener-
89 ation of CCMs.

90 A key challenge in identifying the drivers of age-of-air – and other stratospheric trans-
91 port – biases is that they reflect the time-integrated effects of advection by the residual
92 mean circulation and eddy diffusive mixing, or the quasi-random transport due to the
93 breaking of Rossby waves (e.g., Holton et al. (1995); Plumb (2002)). Given that the in-
94 fluences of mixing and advection are not easily separable, studies have come to differ-
95 ent conclusions about sources of age biases in models. In particular, the analysis of the
96 CCMVal models showed a strong correlation between the intermodel spread in the age-
97 of-air and lower stratospheric tropical upwelling, whereas Dietmüller et al. (2018) showed
98 that the age spread among the CCMI models was driven by differences in mixing. While
99 future attempts to further distinguish between sources of age biases using either simpli-
100 fied “leaky pipe” models (Plumb (1996); J. L. Neu and Plumb (1999)) or more complete
101 measures of the transport circulation such as the “age spectrum” (e.g., Hall and Plumb
102 (1994); Waugh and Hall (2002))) may prove enlightening, at present there is no consen-
103 sus on what is causing large simulated age-of-air biases in models.

104 One potential limitation of previous work based on multi-model intercomparisons
105 is that many aspects of model formulation can influence both stratospheric upwelling and
106 mixing. Thus, while intercomparisons are useful for identifying common model biases,
107 understanding the drivers of these biases is difficult absent single model-based process
108 studies. Among these, several aspects of model formulation have been identified as in-
109 fluencing simulated mean age distributions. As the mean age is sensitive to vertical mo-
110 tion in the lowermost stratosphere, these include large sensitivities to vertical resolution
111 (Orbe et al. (2020)) and to spurious vertical mixing either introduced in vertical coor-
112 dinate transformations in offline chemical transport models (B. Monge-Sanz et al. (2007))
113 or through use of assimilated winds performed either in offline (e.g., Legras et al. (2004))
114 or online data assimilation and “nudged” configurations (e.g., Pawson et al. (2007); Orbe
115 et al. (2017); Davis et al. (2022)). These age sensitivities can be still further amplified,
116 depending on whether or not parameterized gravity waves are included (Eichinger et al.
117 (2020)).

118 By comparison, sensitivities of the mean age to underlying tracer numerics have
119 been less well examined, although Eluszkiewicz et al. (2000) documented a large sensi-

120 tivity in simulated age-of-air values to the choice of advection scheme. More recently,
 121 Gupta et al. (2020) showed differences of $\sim 25\%$ in the age-of-air across identical exper-
 122 iments performed using four different dynamical cores, especially between those using
 123 spectral versus finite-volume schemes. The experiments employed in that study, how-
 124 ever, were highly idealized and it is not clear if the strong influence of tracer numerics
 125 that they identified is also realized in more comprehensive model simulations with moist
 126 physics, especially in the context of model development as carried out in operational mod-
 127 eling centers.

128 To better elucidate this influence of tracer numerics on the transport properties sim-
 129 ulated in a comprehensive global model context, here we document the sensitivity of the
 130 stratospheric mean age in several recent versions of the NASA Global Earth Observing
 131 System (GEOS) general circulation model (Molod et al., 2015). The versions examined
 132 here represent different stages in model development since the Modern-Era Retrospec-
 133 tive Analysis for Research and Applications Version 2 (MERRA-2; Gelaro et al. (2017)).

134 Our focus on transport evaluation is partly in wake of the upcoming release of the
 135 GEOS Retrospective analysis for the early 21st Century (GEOS-R21C), which is an at-
 136 mospheric reanalysis that includes many advances over MERRA-2, and serves as a step
 137 towards MERRA-3, a planned coupled Earth system reanalysis. Along with having im-
 138 plications for GEOS-R21C, our analysis also includes the GEOS-IT Version 5.29.4 dat-
 139 ing from October 19, 2022 (hereafter simply “GEOS-IT”), which will be used to drive
 140 an off-line chemistry reanalysis with a full chemistry model (GEOS-Chem) and an ad-
 141 vanced Constituent Data Assimilation component to update the chemistry fields. Since
 142 this chemical reanalysis will be produced in replay-mode (one-way coupling) whereby
 143 the meteorology fields are used to define the background atmospheric flow (Orbe et al.,
 144 2017), it is imperative that recent tags of GEOS produce a credible representation of trans-
 145 port processes.

146 In particular, here we document how in the process of evaluating candidate sys-
 147 tems for GEOS-R21C we found that the mean age was ~ 1 year younger (or $\sim 30\%$ smaller)
 148 than the values simulated in the model version used to produce MERRA-2 (Figure 1).
 149 The model versions shown in Figure 1 reflect more than 10 years’ worth of accumulated
 150 changes in model development, most notably changes in radiation, parameterized con-
 151 vection and, as we focus on here, changes in the model’s description of vertical advec-
 152 tion. More precisely, we show that slight modifications to the so-called “remapping” al-
 153 gorithm, which is used to transform advected fields from Lagrangian levels to the new
 154 pressure levels after each horizontal advection time step, are the primary driver of the
 155 age-of-air changes exhibited in recent GEOS-R21C candidate model versions. Thus, whereas
 156 Gupta et al. (2020) highlighted large differences between dynamical cores employing spec-
 157 tral versus finite-volume (FV) numerics, our results show that large transport differences
 158 can occur even within a given FV dynamical core, a result which may have broader im-
 159 plications for other general circulation models employing FV numerics. We begin by dis-
 160 cussing methods in Section 2 and present key results and conclusions in Sections 3 and
 161 4, respectively.

162 2 Methods

163 2.1 Model Configurations

164 Here we present results from several versions of GEOS spanning MERRA-2 to more
 165 recent candidates for GEOS-R21C. Among these model versions, a subset are more “of-
 166 ficial” as they have been documented and/or employed in recent model intercomparisons
 167 and are highlighted in Figure 1. In particular, these include a model version that was
 168 used in Phase 1 of CCM1 and documented in Orbe et al. (2017) (Fig. 1, red line). A more

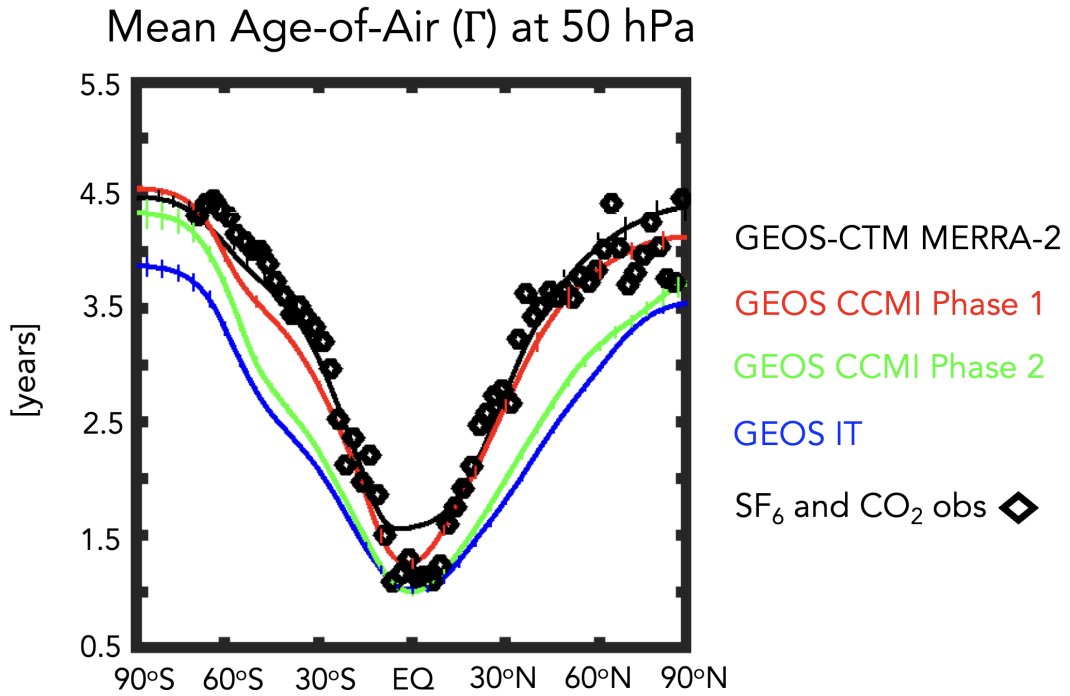


Figure 1. The 2000-2010 climatological annual mean meridional profile of the stratospheric mean age-of-air (Γ), evaluated at 50 hPa. Results from a GEOS-CTM integration constrained with MERRA-2 meteorological fields (black line) as well as free-running GEOS simulations using a model configuration for CCM1 Phase 1 (red line), CCM1 Phase 2 (green line) and the GEOS-IT Version 5.29.4 dating from October 19, 2022 (hereafter simply "GEOS-IT", blue line) are shown. All simulations are constrained with the same (observed) historical sea surface temperatures. Diamonds correspond to SF₆ and CO₂ in situ based estimates of Γ from Boering et al. (1996) and Engel et al. (2009). Vertical dashed lines denote $\pm\sigma$, the standard deviation of Γ over 2000-2010, for each model simulation.

169 recent model version that was used in the CCMI Phase 2 simulations (correspondence
170 with Michael Manyin) is also shown (Fig. 1, green line).

171 We begin by comparing 10-year (2000-2010) climatological mean zonally averaged
172 age-of-air profiles at 50 hPa across this subset of model versions, derived from 30-year
173 long atmosphere-only (AMIP) integrations constrained with observed sea surface tem-
174 peratures (Figure 1). First, we note that the profiles for the CCMI Phase 1 version of
175 the model are very close to observations (black stars), consistent with the
176 “GEOSCCM” documented age characteristics reported in Dietmüller et al. (2018) (see
177 their Figure 3). In addition, while passive tracers were not integrated within MERRA-
178 2, results using the GEOS chemistry transport model (GEOS-CTM, Kouatchou et al.
179 (2015)) constrained with MERRA-2 meteorological fields (black line) also exhibits good
180 agreement with observed values. This good agreement between the CTM-generated age-
181 of-air and the observations is consistent with results from a previous GEOS-CTM sim-
182 ulation (constrained with MERRA) as documented in Orbe et al. (2017).

183 Moving to more recent development versions of the model (green and blue lines),
184 however, reveals a reduction in the mean age by ~ 1 year over both southern and north-
185 ern high extratropical latitudes, or a decrease of $\sim 20\text{-}30\%$ relative to the MERRA-2 con-
186 strained simulation and the observations. As discussed earlier, the green line refers to
187 the CCMI Phase 2 model version, whereas the blue line refers to GEOS-IT. Note that
188 this decrease in the climatological age in both model versions far exceeds the (internal)
189 variations in mean age that occur interannually (vertical bars on solid lines).

190 Since MERRA-2, numerous updates have been introduced in to the GEOS model.
191 This includes replacing the Chou Suarez (Chou & Suarez, 1994) and Chou (Chou, 1990,
192 1992) radiation codes with the Rapid Radiative Transfer Model for GCMS (RRTMG;
193 Iacono et al. (2008), which impacts the stratosphere; the introduction of the Grell-Freitas
194 deep-convection code (Grell and Freitas (2014); Freitas et al. (2018)), which has a min-
195 imal impact on this study; and the upgrade from the GMAO FV core of Lin (2004) to
196 the GFDL FV3 dynamical core (Lin et al., 2017).

197 As we show in Section 3, the latter transition from the GMAO FV to the GFDL
198 FV3 core has the largest impact on the simulated age-of-air values. This degradation in
199 simulated transport within the GFDL FV3 core primarily reflects differences in the im-
200 plementation of the remapping algorithm, which is used to vertically interpolate indi-
201 vidual material surfaces after each horizontal advection step back to the model’s refer-
202 ence Eulerian coordinate. In its implementation in MERRA-2 within the GMAO FV core
203 (Table 1), this remapping involves 1) fitting piecewise parabolic (hereafter PPM) func-
204 tions to input layer-mean values of U , V , Q and tracers; 2) calculating PPM functions
205 to output layer edges; 3) integrating PPM functions between output layer edges to pro-
206 duce new layer-mean values of U , V , Q and tracers; 4) calculating total energy (TE) at
207 input mid-layer pressures; 5) calculating TE at output mid-layer pressures using cubic
208 interpolation and applying an a-posteriori integral conservation; and, finally, 6) remap-
209 ping temperatures from total energy via $T = (TE - K - \Phi)/C_p$. Here T , U , V , Q , C_p ,
210 K and Φ correspond to temperature, zonal wind, meridional wind, specific humidity, spe-
211 cific heat capacity and kinetic and potential energy, respectively.

212 When implemented within the GFDL FV3 core this remapping algorithm yields
213 degradations in simulated stratospheric transport. As the two dynamical cores are too
214 different to meaningfully compare in an apples-to-apples fashion, we use targeted exper-
215 iments with the GMAO FV core to show that the degradations in simulated transport
216 in the GFDL FV core resemble changes that occur when using a lower order (quadratic
217 vs. cubic) interpolation scheme in Step 5 of the remapping algorithm (Table 1). This
218 otherwise innocuous change in interpolation order in turn highlights the large sensitiv-
219 ities in transport that can occur even *within* a given finite-volume numerical scheme, in

Table 1. GMAO Core Finite-Volume Remapping Algorithm: The remapping algorithm examined in this study controls how individual material surfaces are vertically interpolated back to standard pressure levels. Employing linear – and to a lesser extent – quadratic interpolation in Step 5 produces stratospheric transport characteristics that are more consistent with the most recent GEOS model configurations (green and blue lines, Figure 1), whereas a cubic interpolation is more consistent with older configurations (red and black lines, Figure 1) and with MERRA-2. Here T , U , V , Q , C_p , K and Φ correspond to temperature, zonal wind, meridional wind, specific humidity, specific heat of air at constant pressure and kinetic and potential energy, respectively.

Step	REMAP Procedure (MERRA-2, GMAO FV Core)
1	Fit PPM functions to input layer-mean U , V , Q and tracers
2	Calculate PPM to output layer edges
3	Integrate PPM functions between output layer edges to produce new layer-mean U , V , Q and tracers
4	Calculate $TE = C_p T + K + \Phi$ at input mid-layer pressures
5	Calculate TE at output mid-layer pressures using cubic interpolation and a-posteriori integral conservation
6	Construct “remapped” T via $T = (TE - K - \Phi)/C_p$

220 our case resulting in large differences in lower stratospheric upwelling and a $\sim 30\%$ re-
 221 duction in the simulated mean age of air.

222 **2.2 Model Experiments**

223 **2.2.1 AMIP vs. EMIP**

224 We begin our analysis by interpreting the results shown in Figure 1, which are all
 225 based on historical AMIPs that were performed at the same cubed sphere C180 (approx-
 226 imately half-degree) horizontal resolution. As they represent more official model versions
 227 they serve as an important motivation for the experiments that follow. However, there
 228 are numerous (potentially compensating) development changes between these model ver-
 229 sions which renders it nearly impossible to cleanly identify drivers of differences in their
 230 simulated transport.

231 To this end, in order to investigate the drivers of the differences in Figure 1 we per-
 232 form targeted modeling experiments aimed at disentangling the influence of individual
 233 model development changes on stratospheric transport properties (Table 2). In order to
 234 evaluate impacts on transport climate statistics, we consider both a set of climatolog-
 235 ical AMIP (rows 1-4) as well as so-called “EMIP” (rows 5-7) experiments.

236 In particular, we carry out 30-year-long AMIP simulations at C180 resolution which
 237 we use to infer the climate characteristics of the different model configurations. The “EMIP”
 238 experiments – ensembles of 3-month-long integrations initialized on approximately Novem-
 239 ber 15 of each year between 1985 and 2015 – are also used to infer impacts on simulated
 240 transport climate. As they are more computationally efficient than AMIPs since all 30
 241 3-month integrations may be run in parallel, they are performed at both C180 and C360

Table 2. GEOS Model Experiments: Targeted GEOS model experiments based off a control experiment (row 1) were carried out to identify the influence of radiation (row 2) and changes in the remapping algorithm used since MERRA-2 (row 3), as well as their combined influence (row 4). The influence of the remapping algorithm changes is then interpreted using a simpler set of sensitivity experiments, performed using the GMAO FV core, in which only the order of the interpolation scheme used to calculate TE at output mid-layer pressure levels is altered (rows 5-7). Experiments in rows 1-4 are 30-year-long AMIPs run at C180 resolution, whereas rows 5-7 refer to 30-member 3-month-long (DJF) EMIP experiments. Both AMIPs and EMIPs are used for climate statistic evaluation (see Appendix B for more on the correspondence between the two). EMIP experiments are run at both C180 and C360 horizontal resolutions.

Experiment Name	Configuration	Experiment Type	Hor. Resolution
CTRL	Control, FV3 Core	AMIP (30 yrs.)	C180
CSRAD	Chou-Suarez (1994) Radiation (RAD)	AMIP (30 yrs.)	C180
M2REMAP	GMAO FV Core (cubic)	AMIP (30 yrs.)	C180
CSRAD+M2REMAP	Chou-Suarez (1994) RAD GMAO FV Core (cubic)	AMIP (30 yrs.)	C180
LINEAR	GMAO FV Core (linear)	EMIP (30 mem.)	C180, C360
QUADRATIC	GMAO FV Core (quadratic)	EMIP (30 mem.)	C180, C360
CUBIC	GMAO FV Core (cubic)	EMIP (30 mem.)	C180, C360

242 (approximately quarter-degree) resolutions in order to examine the sensitivity of our re-
243 sults to changes in horizontal resolution.

244 As shown in Appendix B, comparisons of the December-January-February (DJF)
245 vertical profile of tropical upwelling show excellent agreement between EMIP and AMIP
246 integrations carried out using the same model configuration (Appendix Figure B1). This
247 somewhat incidental result represents, to the best of our knowledge, the first time that
248 EMIP-based statistics have been shown to converge well to those from AMIPs for the
249 stratospheric metrics considered in this study. This suggests that EMIPs, relative to AMIPs,
250 may be used to provide a computationally more efficient initial assessment of the impacts
251 of model changes on the stratospheric circulation.

252 *2.2.2 Model Development Changes*

253 Moving next to the precise model development changes examined, we begin by defin-
254 ing a control experiment (CTRL; Table 2, row 1), which best corresponds to the blue
255 line shown in Figure 1. Then we define three new AMIP experiments, which aim to dis-
256 tinguish between the age-of-air changes resulting from changes in radiation versus changes
257 in the handling of the REMAP algorithm that occurred in the transition from the GMAO
258 to the FV3 cores (Section 3.2.1).

259 Specifically, these include experiments in which we a) replace RRTMG with the ra-
260 diation from Chou and Suarez (1994) (CSRAD; Table 2, row 2), b) replace the current
261 FV3 REMAP approach with the settings used in the GMAO FV core when running MERRA-
262 2 (i.e., M2REMAP; Table 2, row 3) and c) combine these two changes (CSRAD+M2REMAP;
263 Table 2, row 4).

264 As we show in Section 3.2.1, the M2REMAP experiment produces the largest changes
265 in age-of-air, compared to the experiment in which only the radiation is altered. Inter-

266 preting this result, however, is not straightforward since there are several differences in
 267 the implementation of the remapping algorithm between the GMAO and FV3 cores that
 268 are interdependent and, thus, difficult to isolate cleanly. To this end, in order to simplify
 269 the problem we focus the remainder of our investigation (Section 3.2.2) on examining
 270 a clean set of EMIP experiments that are all performed using the GMAO FV core and
 271 that differ from each other only in terms of the order of the interpolation that is used
 272 to calculate TE at the mid-layer pressure levels (Step 5, Table 1). More precisely, we com-
 273 pare configurations using a linear (LINEAR; Table 2, row 5), quadratic (QUADRATIC;
 274 Table 2, row 6) and cubic interpolation (CUBIC; Table 2, row 7) scheme, with the lat-
 275 ter corresponding to the approach that was used in MERRA-2. To assess the robustness
 276 of our findings to changes in horizontal resolution, all three sensitivity experiments are
 277 run at both C180 and C360 resolutions.

278 These three numerical schemes are derived from the generic Lagrangian interpo-
 279 lation equation:

$$\mathcal{Q}(\mathcal{P}) = \sum_{k'} a_{k+k'} \mathcal{Q}_{k+k'} \quad k' = 0, \pm 1, \pm 2, \dots \quad (1)$$

280 where \mathcal{P} represents the target output location in $\ln(p)$ and $\mathcal{Q}_{k+k'}$ denotes the surround-
 281 ing grid-point values at input locations. The coefficients $a_{k+k'}$ are derived through Tay-
 282 lor Series expansions using non-uniform grid spacing given by:

$$a_{k+k'} = \frac{\prod_m (\mathcal{P}_{k+m} - \mathcal{P})}{\prod_m (\mathcal{P}_{k+m} - \mathcal{P}_{k+k'})} \quad m = 0, \pm 1, \pm 2, \dots \quad m \neq k' \quad (2)$$

283 For the three schemes, the grid points used are: LINEAR ($k, k-1$), QUADRATIC ($k+$
 284 $1, k, k-1$), and CUBIC ($k+1, k, k-1, k-2$). In all cases, the grid points are chosen
 285 such that the target location resides between layers k and $k-1$.

286 Note that, while the LINEAR and QUADRATIC experiments do not actually cor-
 287 respond to any of the model versions shown in Figure 1, they highlight the large sensi-
 288 tivity of the mean age to changes in the interpolation scheme that may otherwise seem
 289 innocuous. They also provide further evidence of the strong influence of changes in tropi-
 290 cal lower stratospheric upwelling strength on the stratospheric mean age in GEOS.

291 Finally, in all experiments using the MERRA-2 remapping approach (i.e., M2REMAP,
 292 CSRAD+M2REMAP, LINEAR, QUADRATIC, CUBIC) additional modifications to the
 293 divergence damping coefficients were used so as to best ensure consistency with what was
 294 used in MERRA-2. Specifically, these include changes to the number of layers for ver-
 295 tical subgrid mixing, the coefficient for barotropic mode damping, the use of 2nd vs. 6th
 296 order divergence damping and the strength of the divergence damping coefficients.

297 **2.3 Analysis Approach**

298 **2.3.1 Transport Diagnostics**

299 To diagnose the transport circulation we focus primarily on the age-of-air (Hall and
 300 Plumb (1994)). This is inferred from an idealized global “clock” or ideal age tracer (Γ)
 301 (Thiele and Sarmiento (1990)) that is defined with respect to the bottom model level
 302 as follows: initially, the ideal age tracer is set to zero throughout the troposphere and
 303 thereafter held to zero over the entire Earth’s surface, subject to a constant aging of 1
 304 year/year throughout the atmosphere. We present here the statistically stationary (equi-
 305 librated) value of $\Gamma(r)$, which is equal to the average time since the air at a location r
 306 in the stratosphere last contacted the Earth’s surface. In addition to the mean age, we
 307 also show results from an idealized e90 tracer that is uniformly emitted over the entire
 308 surface layer and decays exponentially at a rate of 90 days⁻¹ such that concentrations
 309 greater than 125 ppb and less than 50 ppb tend to reside in the lower troposphere and
 310 stratosphere, respectively (Prather et al. (2011)). As this tracer features strong near-

311 tropopause gradients and takes significantly less time to equilibrate, compared to the mean
 312 age, it is useful for evaluating stratosphere-troposphere-exchange and transport within
 313 the upper troposphere/lower stratosphere (Abalos et al. (2017, 2020); Orbe et al. (2020)).

314 Both the mean age and e90 tracers were integrated in all of the AMIP experiments
 315 shown in Figure 1 and listed in Table 2 (rows 1-4), which were run using the same ideal-
 316 ized passive tracer package described in Orbe et al. (2017). Note that the mean age
 317 tracer was not integrated in the EMIP experiments given its much longer characteris-
 318 tic timescale in the stratosphere (~ 3 -5 years). As such, the EMIP simulations, which
 319 do not exceed one year, are not appropriate for evaluating the time-integrated transport
 320 characteristics reflected in the age-of-air.

321 In addition to carrying the idealized tracers, two of the experiments shown in Fig-
 322 ure 1 were also run with full interactive chemistry and correspond to the two CCMI (Phase
 323 1 and Phase 2) integrations (red and green lines, Figure 1). Both simulations employ the
 324 same Global Modeling Initiative (GMI) chemical mechanism (Strahan et al. (2013)) and
 325 are therefore useful in evaluating the impact of age differences on real trace gas distri-
 326 butions. In particular, as shown in Section 3.1 results from these experiments show sig-
 327 nificant imprints of the age-of-air changes on nitrous oxide (N_2O) and methane (CH_4).

328 **2.3.2 Circulation Diagnostics**

329 As we show in Section 3, the changes in age-of-air across the different model ver-
 330 sions are strongly tethered to changes in the advective component of the circulation, which
 331 we quantify using the Transformed Eulerian Mean (TEM) estimate of the Lagrangian
 332 transport of mass by the circulation. Thus, in addition to more standard Eulerian met-
 333 rics of the circulation (e.g., zonal winds and temperatures), we focus on the vertical com-
 334 ponent of the TEM residual velocity, defined as $\bar{w}^* = \bar{w} + \frac{\partial(\psi \cos \phi)}{\partial \phi}$, where $\psi = \overline{v'\theta'}/\frac{\partial \theta}{\partial p}$
 335 is the eddy stream function, θ refers to potential temperature, a is the Earth's radius
 336 and overbars and primes denote zonal means and deviations therefrom, respectively (Andrews
 337 et al. (1987)). In addition, we interpret the behavior in w^* using the Eliassen-Palm flux
 338 divergence ($\nabla \cdot \mathbf{F}$), whose horizontal ($\mathbf{F}(\phi)$) and vertical ($\mathbf{F}(p)$) components are respec-
 339 tively defined as $\mathbf{F}(\phi) = \overline{a \cos \phi [\frac{\partial u}{\partial p} \psi - u'v']}$ and $\mathbf{F}(p) = \overline{a \cos \phi [f - \frac{\partial u \cos \phi}{\partial \phi}] \psi - u'w'}$.

340 **2.4 Observations and Reanalyses**

341 While our focus is on interpreting and understanding the different model config-
 342 urations, we incorporate observations to provide context when possible, although we do
 343 not present an exhaustive evaluation of the model's transport characteristics (for that
 344 see earlier studies including Orbe et al. (2017, 2018)). However, as the tracers are not
 345 directly integrated in MERRA-2 (with the exception of ozone), we compare against in-
 346 dependent observational estimates. For the mean age we first compare simulated merid-
 347 ional age profiles at 50 hPa with values derived from in situ aircraft measurements of car-
 348 bon dioxide (CO_2), averaged in 2.5 degree latitude bins over the altitude range 19.5 to
 349 21.5 km (Boering et al. (1996), see also Figure 5 in Hall et al. (1999)).

350 We also briefly evaluate impacts of transport biases on the simulated trace gas dis-
 351 tributions for the CCMI Phase 1 and 2 experiments. The simulated fields of methane
 352 (CH_4) are compared with the climatologies derived for 1991–2002 from the Halogen Oc-
 353 cultation Experiment (HALOE) on board the Upper Atmosphere Research Satellite (UARS)
 354 (Grooß and Russell III (2005)). Comparisons of simulated nitrous oxide (N_2O) are made
 355 against climatologies derived from the Microwave Limb Sounder (MLS) on the Earth Ob-
 356 serving System (EOS) Aura satellite. Climatologies over the same period (2005–2015)
 357 are used to evaluate both the model and the observations. We use the 190-GHz retrieval
 358 from Version 4.2 because the 640-GHz data set ends in summer 2013 due to the failure
 359 of the N_2O primary band.

DJF Climatological Mean Tropical Upwelling (w^*)

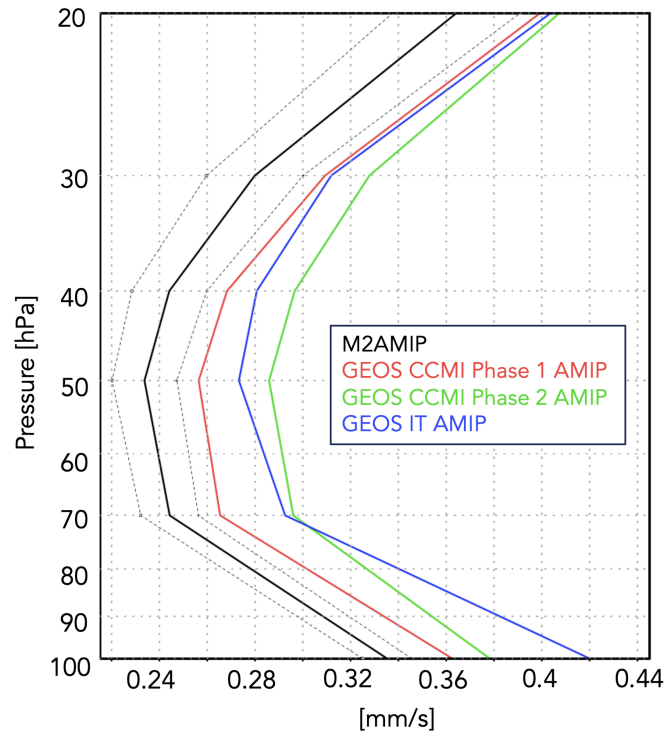


Figure 2. The DJF 1985-1994 climatological mean vertical residual mean velocity, w^* , averaged at each level between the turnaround latitudes for GEOS free-running AMIP simulations using the model configurations corresponding to the CCMI Phase 1 (red) and Phase 2 (green) submissions and to GEOS-IT (blue). M2AMIP is shown in black, with black dashed lines denoting ± 1 standard deviation.

360 For the circulation diagnostics nearly all comparisons are made relative to the MERRA-
 361 2 data assimilation (DAS) reanalysis product, noting that comparisons against ERA-5
 362 (not shown) reveal a similar picture. One exception, however, is the vertical component
 363 of the TEM circulation (w^*), which shows some differences in vertical structure between
 364 the MERRA-2 DAS and a 30-member ensemble of (free-running) AMIP integrations pro-
 365 duced using the MERRA-2 model, hereafter referred to as M2AMIP (Collow et al., 2017)(Ap-
 366 pendix Figure A1, right). As the free-running model results shown in Figure 1 show more
 367 consistency with the vertical profile of M2AMIP, not MERRA-2, we compare w^* in all
 368 free-running GEOS experiments with M2AMIP, noting that for non-derived measures
 369 (i.e., winds, temperatures), the raw MERRA-2 output is used.

370 The differences in w^* between M2AMIP and the MERRA-2 DAS may reflect the
 371 influence of temperature increments in the DAS (MERRA-2) which can drive spurious
 372 vertical transport in assimilated products (Weaver et al., 1993; Orbe et al., 2017). In par-
 373 ticular, Weaver et al. (1993) showed that the imbalance between the thermal and veloc-
 374 ity fields at the time an observation is ingested during the assimilation cycle can excite
 375 unwanted inertial-gravity wave modes that manifest strongly in the residual vertical winds.
 376 While this impact of the increments may explain the differences in w^* , we reserve a more-
 377 in depth examination for future work as our focus is on the transport characteristics of
 378 the free-running GEOS system.

379 3 Results

380 3.1 Reduction of Stratospheric Mean Age in GEOS Models 381 Since MERRA-2

382 We begin by interpreting the reduction in mean age exhibited in more recent model
 383 versions in terms of changes in the strength of upwelling in the tropical lower stratosphere.
 384 In particular, the reductions in Γ (Figure 1) are consistent with increases in the strength
 385 of lower stratospheric tropical upwelling, with w^* becoming progressively stronger in more
 386 recent model versions, relative to MERRA-2 (Figure 2). Note that these increases in w^*
 387 across model versions exceed those due to internal variability alone (black dotted lines,
 388 Fig. 2). Furthermore, while the increases in w^* occur throughout the stratosphere, we
 389 focus on the changes occurring between 70 and 100 hPa as these are most relevant to
 390 determining the tropical upward mass flux and associated strength of the mean overturn-
 391 ing circulation.

392 Though perhaps naive, the relationship between lower stratospheric upwelling and
 393 the mean age suggested by comparing Figure 1 and Figure 2 is consistent with the long-
 394 term behavior of Γ inferred from both historical and projected future climate simulations
 395 (Butchart et al. (2010); Abalos et al. (2021)). A strong relationship between the strength
 396 of lower stratospheric ascent and the mean age was also shown to hold in the CCMVal
 397 models (see Fig. 5.20 in J. Neu et al. (2010)). Nevertheless, it is important to note that
 398 a clear relationship between w^* and Γ is not a priori expected, as the age-of-air is also
 399 known to be very sensitive to mixing, which may be important in interpreting differences
 400 among the CCM Phase 1 models (Dietmüller et al. (2018)).

401 The differences in w^* highlighted in Figure 2 are associated with enhanced Eliassen-
 402 Palm flux convergence over NH midlatitudes (Figure 3). Increased wave convergence is
 403 evident not only within the subtropical lower stratosphere ($< 30^\circ\text{N}$, 50-100 hPa) but also
 404 over higher latitudes and altitudes ($\sim 40^\circ\text{-}70^\circ\text{N}$, 20-50 hPa). The fact that differences
 405 in extratropical wave convergence imprint on tropical upwelling is consistent with our
 406 understanding of the so-called “downward control” principle (Haynes et al. (1991)).

407 In particular, the strength of the residual mean streamfunction (Ψ^*) is, via down-
 408 ward control, directly related to the vertically integrated eddy-induced total zonal force
 409 above that level and has contributions both from the (resolved wave) Eliassen-Palm flux

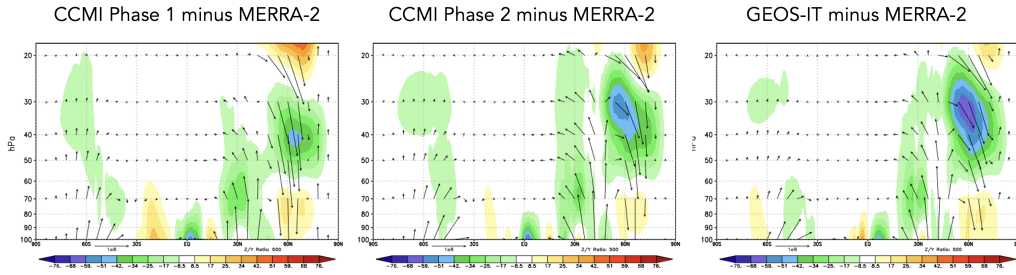
DJF Climatological Mean Eliassen-Palm Flux Divergence ($\nabla \cdot \mathbf{F}$)

Figure 3. Colors show anomalies in the DJF climatological mean Eliassen-Palm (EP) flux divergence between the CCMI Phase 1 (left), CCMI Phase 2 (middle) and GEOS-IT AMIP (right) model versions, relative to MERRA-2. Arrows denote anomalies in the vertical and meridional EP flux vectors (relative to MERRA-2).

410 divergence (Figure 3) as well as the gravity wave drag scheme’s parameterized waves (not
 411 shown). The tropical upward mass flux – defined as $\Psi_{\max}^* - \Psi_{\min}^*$ evaluated at the turnaround
 412 latitudes (e.g. Rosenlof (1995)) – is therefore directly dependent on the wave forcing aloft.

413 One subtlety to note is that the wave convergence changes shown in Figure 3 oc-
 414 cur at high latitudes and are directly associated with downwelling over the polar region.
 415 It is then via mass balance that anomalously strong downwelling associated with enhanced
 416 flux convergences must be accompanied by enhanced upwelling in the tropics. This in-
 417 direct impact of higher latitude wave drag reflects an “extratropical pumping” mecha-
 418 nism (Holton et al., 1995), which is illustrated more clearly in Section 3.2.2 in the con-
 419 text of the LINEAR, QUADRATIC and CUBIC experiments.

420 While the reduction in Γ (Figure 1) of $\sim 30\%$ at 50 hPa is significant, it is neither
 421 clear if this change is representative of other altitudes within the stratosphere nor how
 422 this age bias imprints on real chemical species. To this end, we begin by comparing the
 423 full latitude-pressure distribution of changes in Γ and another passive tracer (e90) (Fig-
 424 ure 4) between the CCMI Phase 1 and Phase 2 model configurations (red and green lines,
 425 Figure 1). In particular, we find that the changes in both passive tracers – large reduc-
 426 tions in Γ within both hemispheres (Fig. 4, top right) and increased values of e90 within
 427 the lower stratosphere (Fig. 4, bottom right) – are reflective of an overall increase in the
 428 strength of the transport circulation. This is highlighted in the CCMI Phase 2 – 1 model
 429 differences for the passive tracer distributions (Fig. 4, right panels) which are shown in
 430 the absence of robust observational constraints of Γ at higher altitudes (or any obser-
 431 vational constraints for e90, for that matter). The reduced/increased stratospheric bur-
 432 dens of the age and e90 tracers are consistent with stronger upwelling in the CCMI Phase
 433 2 model configuration (Figure 2).

434 While the observational constraints on Γ presented in Figure 1 and the departure
 435 of w^* away from MERRA-2 suggest that transport properties of the newer model con-
 436 figurations are moving in the wrong direction, it is relevant to ask whether or not the
 437 trace gas satellite measurements also support this conclusion. Indeed, comparisons with
 438 observations show larger biases in N_2O (Fig. 5, top panels) and CH_4 (Fig. 5, bottom pan-
 439 els), increasing from 10% to 30% in the CCMI Phase 2 model configuration, depending
 440 on the species. Recall that the same chemistry mechanism is used in both CCMI Phase
 441 1 and 2 simulations.

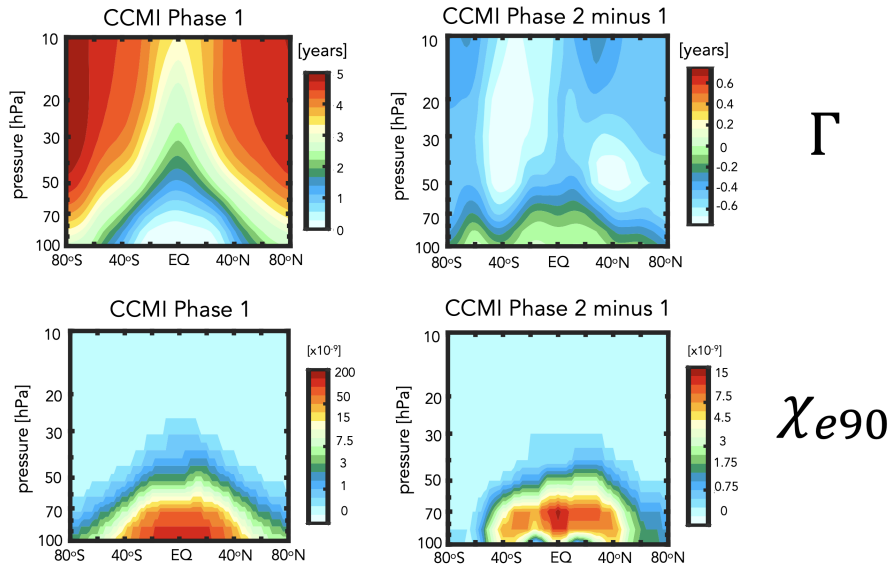


Figure 4. The climatological mean (2000-2010) distribution of the mean age-of-air (Γ) (left, top) and e90 idealized tracers (left, bottom) for the CCMI Phase 1 model configuration. Climatological differences between the CCMI Phase 2 and Phase 1 model configurations are shown in the right panels. Note that a nonlinear colorbar has been used in the e90 subplots.

442 The patterns of the trace gases biases are generally consistent with the biases in
 443 the mean age (Fig. 4). This comports with well-known correlations between the mean
 444 age and stratospheric trace gases, reinforcing the fact that model transport inaccuracies
 445 can significantly affect simulations of important long-lived chemical species in the strato-
 446 sphere (Hall et al. (1999)).

447 The fact that the mean age changes have a significant imprint on the simulated trace
 448 gases is consequential for the GEOS-R21C system. However, the configurations shown
 449 in Fig. 1-5 differ in many respects (physics, resolution, radiation, FV remapping algo-
 450 rithm) and it is difficult to meaningfully interpret what is driving the changes in w^* (and
 451 the tracers). We therefore move next to the targeted model experiments (Table 2) in or-
 452 der to interpret the model development steps that resulted in these transport circula-
 453 tion changes.

454 **3.2 Identifying Drivers of Upwelling and Tracer Changes Since** 455 **MERRA-2**

456 **3.2.1 Radiation versus REMAP Algorithm**

457 As discussed in Section 2, among the model changes that were made since MERRA-
 458 2, the changes in radiation and the FV remapping algorithm are most likely to directly
 459 have impacted the stratospheric circulation. We therefore begin by assessing which of
 460 these changes dominates the decreases in Γ shown in Figure 1.

461 Figure 6 shows the distribution of Γ for experiments in which the longwave, short-
 462 wave, and REMAP updates since MERRA-2 have successively been undone. Relative
 463 to the control experiment (CTRL; Table 2, row 1), the transition back to Chou and Suarez
 464 (1994) in the shortwave and Chou (1990, 1992) in the longwave results in an increase in
 465 the mean age of ~ 0.5 years throughout the stratosphere (CSRAD; Table 2, row 2). Though

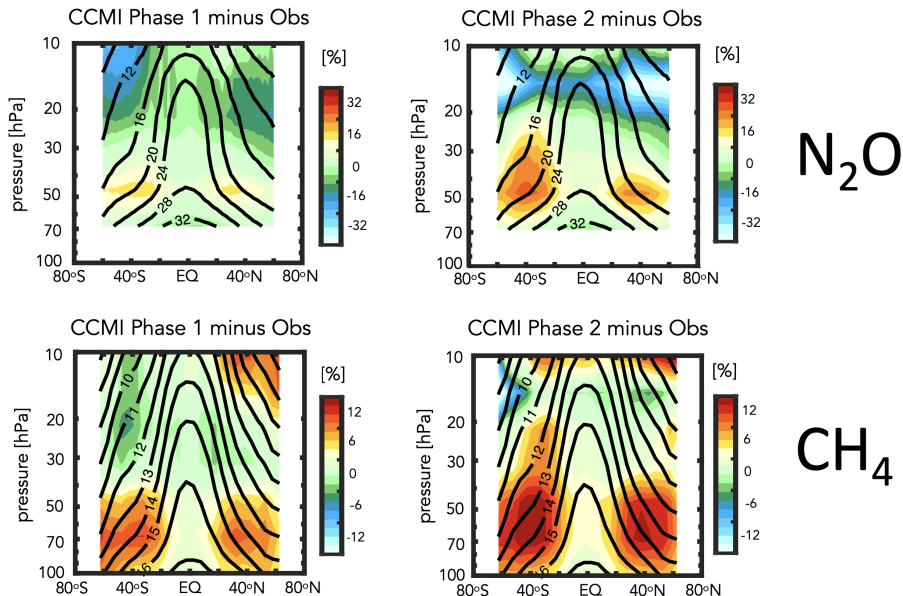


Figure 5. Colors shown anomalies in the simulated distributions of nitrous oxide (N_2O) (top) and methane (CH_4) (bottom), relative to the MLS and HALOE observed values, respectively, for the CCMI Phase 1 (left) and Phase 2 (right) GEOS model configurations. Climatological mean observed values are shown in the black contours.

466 significant, this change in Γ is smaller than the change that results from applying the
 467 remapping approach used in MERRA-2 (M2REMAP; Table 2; row 3), in which the mean
 468 age increases by ~ 1 year. The combined impacts of both changes (CSRAD+M2REMAP;
 469 Table 2 row 4) is roughly linear, with age values of ~ 5.5 years over high latitudes at 50
 470 hPa, consistent with the values simulated by the GEOS-CTM MERRA-2 integration (black
 471 line, Figure 1) and with the CCMI Phase-1 version of the model (red line, Figure 1).

472 Next we ask if the behavior of Γ exhibited in Figure 6 can be interpreted in terms
 473 of changes in the strength of lower stratospheric tropical upwelling and extratropical wave
 474 convergence, as our previous analysis of the CCMI experiments suggested. Indeed, Fig-
 475 ure 7 shows that values of upwelling decrease in the CSRAD and M2REMAP experiments,
 476 relative to the CTRL integration. The increase in upwelling resulting from both changes
 477 (CSRAD+M2REMAP) is still larger, consistent with the larger age decreases in that ex-
 478 periment. This change in the behavior of w^* within the tropical stratosphere can be in-
 479 terpreted in terms of changes in the Eliassen Palm flux convergence over NH midlati-
 480 tudes (not shown), which features smaller values in the CSRAD, M2REMAP (and CSRAD+
 481 MSREMAP) experiments. Note that our examination of the changes in w^* are derived
 482 from EMIP integrations, which we showed previously converge (for DJF) to the statis-
 483 tics derived from corresponding AMIP experiments.

484 It is important to note that, while the reduced values of w^* in the M2REMAP ex-
 485 periment (Fig. 7), represent an improvement, relative to the CTRL integration, these
 486 changes are, in isolation, accompanied by a cold bias ($\sim 4\text{-}6\text{K}$) in the tropical lower strato-
 487 sphere (Fig. 8a). Unlike the upwelling changes, this represents a degradation in model
 488 skill, increasing the temperature bias in that region, relative to MERRA-2 (Fig. 8 b,c).
 489 While this temperature bias is concerning in isolation, it is decoupled from the changes
 490 in residual mean upwelling which, rather, are more sensitive to the changes in *extratrop-*

Annual Climatological Mean Stratospheric Mean Age (Γ)

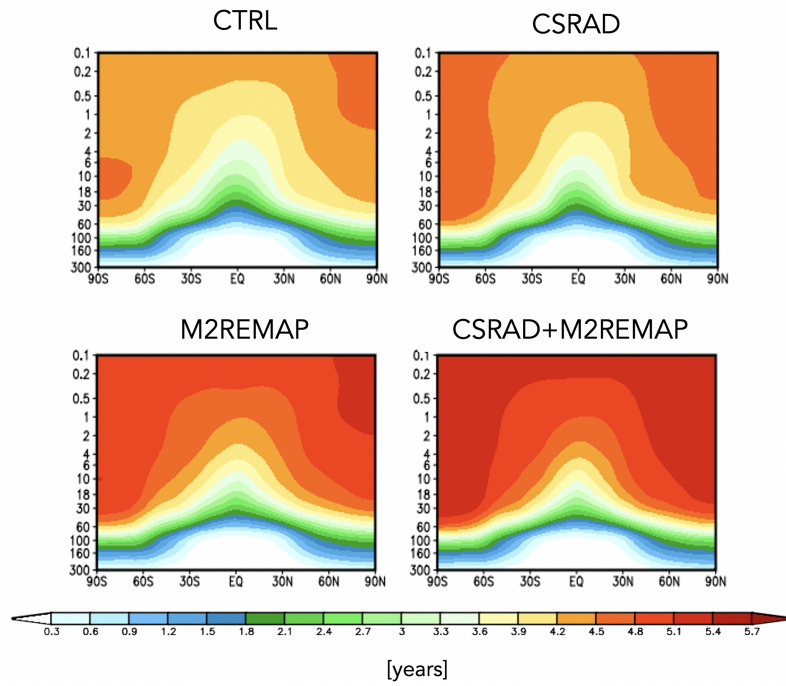


Figure 6. Colors show the simulated 2000-2010 climatological annual mean distributions of the mean age-of-air (Γ) for the CTRL (top left; Table 2, row 1), CSRAD (top right; Table 2, row 2), M2REMAP (bottom left; Table 2, row 3) and combined CSRAD+M2REMAP (bottom right; Table 2, row 4) experiments.

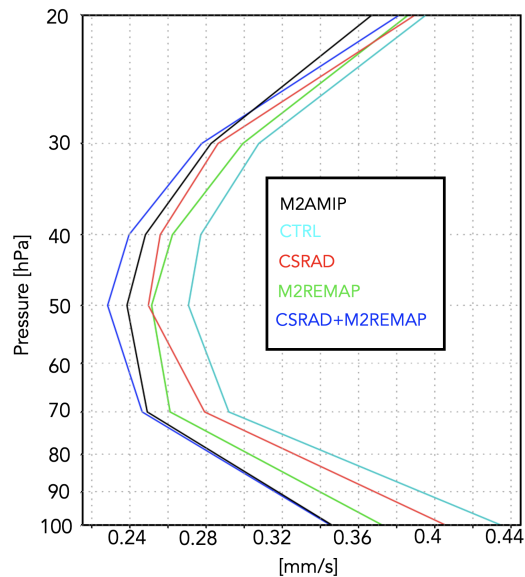
DJF Climatological Mean Tropical Upwelling (w^*)

Figure 7. The DJF 1985-2015 climatological mean vertical residual mean velocity, w^* , averaged at each level between the turnaround latitudes for the CTRL (cyan line; Table 2, row 1), CSRAD (red line; Table 2, row 2), M2REMAP (green line; Table 2, row 3) and combined CSRAD+M2REMAP (blue line; Table 2, row 4) experiments. M2AMIP is shown in black.

491 *ical* wave convergences (described further in the next section). Furthermore, the increased
 492 temperature bias in the M2REMAP experiment appears to be tethered to other updates
 493 that were made in the CTRL model (specifically the radiation progression from Chou-
 494 Suarez to RRTMG). In particular, the M2AMIP ensemble, which also employs the GMAO
 495 cubic remapping option, features a much smaller temperature bias in the tropical lower
 496 stratosphere, relative to MERRA-2 ($\sim 0-2\text{K}$) (Fig. 8d). This suggests that the ampli-
 497 fied temperature bias moving from the CTRL to M2REMAP experiments needs to be
 498 interpreted in the context of other model development changes that were introduced, par-
 499 ticularly in the radiation scheme and its coupling to convection.

500 3.2.2 FV REMAP Algorithm: Sensitivity of Climate Statistics

501 Having shown in the previous section that the largest changes in the mean age were
 502 realized through the differences in implementation of the remapping algorithm between
 503 the GMAO FV core used in MERRA-2 and in current FV3 core configurations, we now
 504 investigate further the sensitivity of the transport circulation to the choice of remapping
 505 interpolation scheme. In particular, we compare simulations run with the GMAO FV
 506 core in which total energy is calculated at new mid-layer pressures using cubic, quadratic
 507 and linear interpolation prior to the aposterior integral conservation (Table 2, rows 5-
 508 7). In addition, in this section we seek to understand how the changes in the Eliassen-
 509 Palm flux convergence over NH midlatitudes arise via analysis of the large-scale wind
 510 structure.

511 **Figure 9** (left panel) shows a clear sensitivity in tropical upwelling to the choice of
 512 interpolation scheme, with w^* progressively increasing in strength moving from the CU-
 513 BIC to QUADRATIC to LINEAR schemes. This sensitivity is robust across horizontal

DJF Climatological Zonal Mean Temperature Anomalies

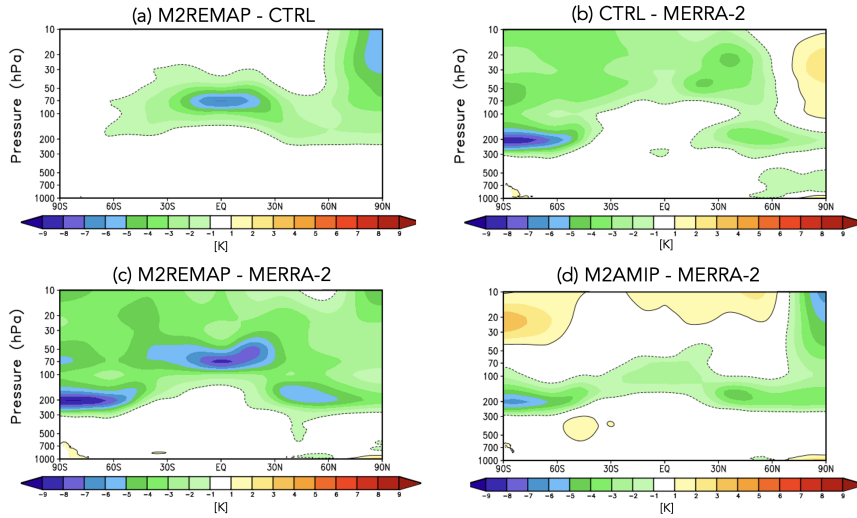


Figure 8. Anomalies in DJF 1985-2015 climatological mean zonal mean temperatures: M2REMAP - CTRL (a), CTRL - MERRA-2 (b), M2REMAP - MERRA-2 (c) and M2AMIP - MERRA-2 (d).

514 resolutions as the same suite of experiments performed at C360 exhibit the same sensi-
 515 tivity (Fig. 9, right panel). While no current model version actually employs a linear
 516 scheme, this suite of experiments highlights the strong sensitivity to choice of interpo-
 517 lation scheme within the remapping algorithm; to the best of our knowledge, this result
 518 has not been reported in the literature.

519 Furthermore, as we show next, this clean set of experiments allow us to inquire mech-
 520 anistically into the processes that are driving the changes in wave convergence over mid-
 521 latitudes, unencumbered by differences in horizontal resolution, physics, etc.

522 Interestingly, the increases in w^* moving from the CUBIC to QUADRATIC schemes
 523 not only manifests in free-running AMIP simulations, but also in AMIP simulations in
 524 which GEOS is constrained (or replayed, following Orbe et al. (2017)) to MERRA-2 me-
 525 teorological fields, using the MERRA-2 GMAO cubic interpolation (Fig. 10, blue line)
 526 and the GFDL FV core remapping approach (Fig. 10, red line). While there is a gen-
 527 eral increase in w^* in the former, however, both simulations, lie within the range of MERRA2-
 528 DAS, suggesting that replay does act to ameliorate some of the upwelling biases man-
 529 ifest in the underlying unconstrained models. While not the focus of this study, this im-
 530 pact of the remapping approach on simulations run in replay mode will be examined fur-
 531 ther in future work.

532 Consistent with our expectations based on the analysis of the previous experiments,
 533 the drivers of the changes in w^* are related to increased wave convergence moving from
 534 the CUBIC to QUADRATIC to LINEAR schemes (Figure 11). Over extratropical lati-
 535 tudes, the zonal force associated with this enhanced wave convergence is associated with
 536 enhanced downwelling at high latitudes that, through mass balance, is accompanied by
 537 enhanced upwelling in the tropics. This indirect impact of higher latitude wave drag is
 538 evident in Appendix Figure C1, which shows stronger upwelling/downwelling in the LIN-
 539 EAR and QUADRATIC experiments over the tropics/polar region.

DJF Climatological Mean Upwelling (w^*)

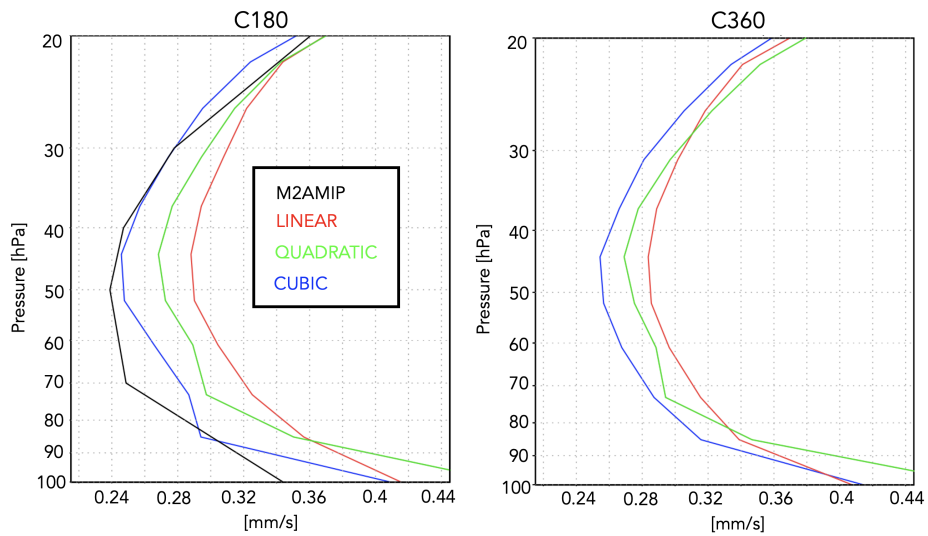


Figure 9. The DJF 1985-2015 climatological mean vertical residual mean velocity, w^* , averaged at each level between the turnaround latitudes for the LINEAR (red line; Table 2, row 5), QUADRATIC (green line; Table 2, row 6) and CUBIC (blue line; Table 2, row 7) experiments. M2AMIP is shown in black. Results from C180 and C360 EMIP experiments are shown in the left and right panels, respectively.

DJF Climatological Mean Tropical Upwelling (w^*)

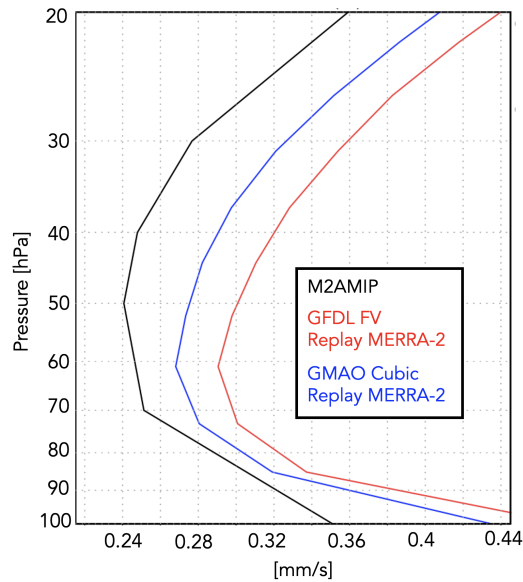


Figure 10. The DJF 2005-2015 climatological mean vertical residual mean velocity, w^* , averaged at each level between the turnaround latitudes for two GEOS replay AMIP simulations constrained with MERRA-2 meteorological fields using remapping approaches from the MERRA-2 GMAO cubic core (blue line) and the GFDL FV core (red line). MERRA-2 DAS is shown in black.

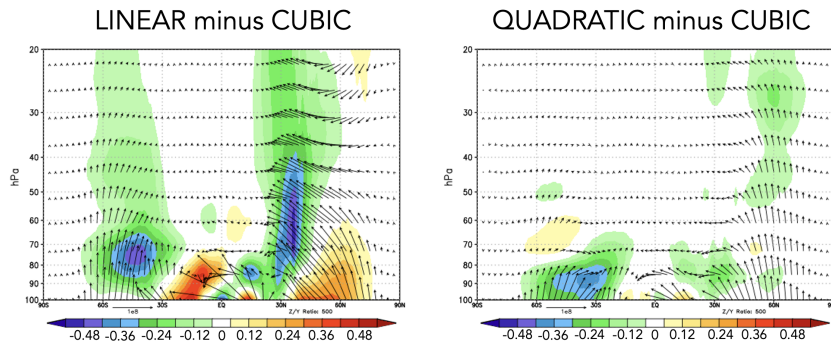
DJF Climatological Mean Eliassen-Palm Flux Divergence ($\nabla \cdot \mathbf{F}$)

Figure 11. Colors shown anomalies in the DJF 1985-2015 climatological mean Eliassen-Palm (EP) flux divergence in the LINEAR (left) and QUADRATIC (right) experiments, relative to the CUBIC model experiment. Arrows denote anomalies in the vertical and meridional EP flux vectors.

540 Next we exploit the fact that these experiments only differ with respect to the in-
 541 terpolation scheme in order to inquire further into the drivers of the wave convergence
 542 changes. To this end, **Figure 12** compares profiles of the zonal mean zonal wind between
 543 the CUBIC, QUADRATIC and LINEAR experiments, averaged over the region of en-
 544 hanced wave convergence (i.e. 20°N-60°N). The experiments featuring stronger wave con-
 545 vergence (LINEAR and QUADRATIC) are also simulations with stronger zonal winds,
 546 relative to MERRA-2, especially above 70 hPa. This change in winds occurs at both C180
 547 (**Fig. 12**, left panel) and C360 (**Fig. 12**, right panel) resolutions.

548 Structurally, the increase in zonal wind strength over northern extratropical mid-
 549 latitudes is reflective of a poleward shift in the zonal winds as the critical latitude, i.e.
 550 where the zonal wind is zero, shifts northward in the QUADRATIC and, especially, LIN-
 551 EAR integrations, relative to the CUBIC experiment (**Figure 13**). Since stationary waves
 552 only propagate in westerly zonal flow, the latitude where zonal flow is zero acts a bound-
 553 ary for wave propagation (Hardiman et al. (2014)). As a result, this shift in critical lat-
 554 itude results in enhanced wave propagation and convergence over middle and high lat-
 555 itudes.

556 **Figures 12 and 13** highlight how the changes in zonal winds in the LINEAR and
 557 QUADRATIC experiments reflect a degradation in model skill, relative to MERRA-2,
 558 throughout the entire stratosphere. The changes in upwelling, mean age, chemical trace
 559 gases and zonal winds thus provide a coherent and self-consistent picture suggestive of
 560 a degradation in the representation of the stratospheric circulation since MERRA-2. That
 561 is, an increased bias in the stratospheric northern zonal winds are, via their influence on
 562 wave convergence, compromising changes in the strength of the mean meridional over-
 563 turning circulation and its impact on composition. It is interesting to note that the wind
 564 biases also extend into the troposphere and show degraded skill relative to MERRA-2
 565 in the LINEAR and QUADRATIC experiments (**Figure 13**). Examination of other fields
 566 (i.e. tropopause biases, Appendix Figure D1) present somewhat more of a nuanced story
 567 that depends on other changes that made to the model since MERRA-2, as shown in **Fig-**
 568 **ure 8 and discussed in Section 3.2.1**. The improvements in the zonal winds, however, are

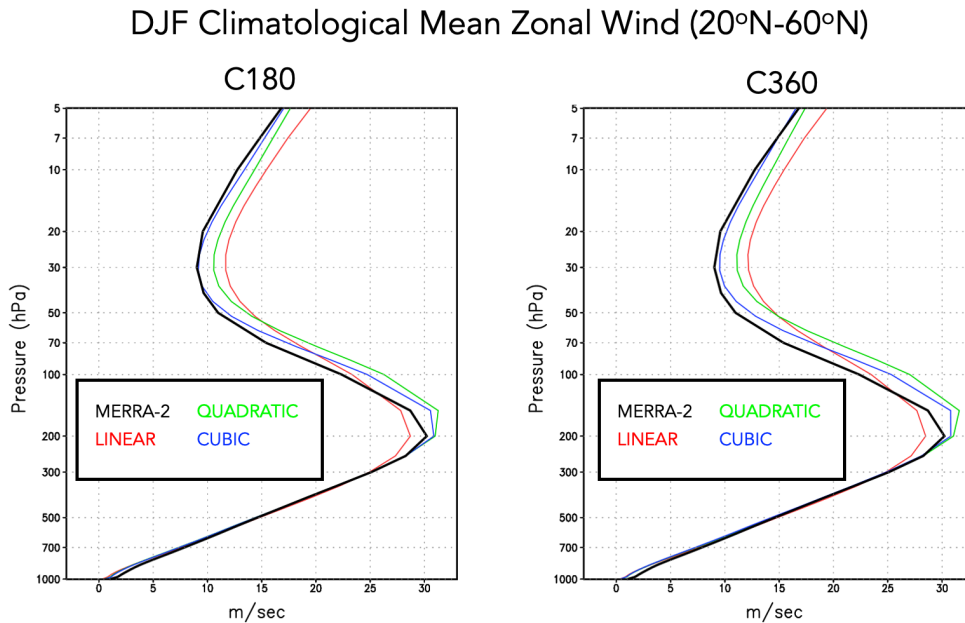


Figure 12. Vertical profiles of the DJF 1985-2015 climatological mean zonal mean zonal winds in the LINEAR (red), QUADRATIC (green) and CUBIC (blue) experiments, averaged between 20°N and 60°N. MERRA-2 is shown in the black line. Results for both C180 (left) and C360 (right) experiments are shown.

569 most relevant for setting the upwelling characteristics within the tropical lower strato-
 570 sphere via their influence on wave propagation into that region.

571 Finally, to better understand why these impacts on the winds have such a conse-
 572 quence for the wave convergence properties within the stratosphere, next we examine the
 573 zonal structure of these biases in the middle stratosphere (Figure 14). This reveals that
 574 the enhanced winds in the LINEAR (and, to a lesser extent, QUADRATIC) integrations
 575 are concentrated over the North Pacific at both C180 (Fig. 14, top) and C360 (Fig. 14,
 576 bottom) resolutions (a similar picture emerges within the troposphere, not shown). As
 577 this region is the primary region dominating the stationary component of the upward
 578 flux of vertical wave activity (Plumb (1985), see their Figure 4) it is perhaps not surpris-
 579 ing that this region is having a profound impact on the mean overturning circulation.
 580 Again, as with the zonal mean wind changes, the increases in wind strength over the North
 581 Pacific represent degraded model skill relative to MERRA-2. Note that comparisons with
 582 ERA-5 reveal a similar bias (not shown).

583 4 Conclusions

584 Here we have performed an analysis aimed at understanding differences in the repre-
 585 sentation of the stratospheric circulation in recent candidate systems for GEOS-R21C,
 586 relative to older versions of GEOS similar to the model used to produce MERRA-2. Us-
 587 ing targeted experiments oriented at disentangling various model development updates,
 588 we have identified a key role played by changes in the implementation of the remapping
 589 algorithm within the model’s finite-volume dynamical core. Our key results are as fol-
 590 lows:

DJF Climatological Zonal Mean Zonal Wind Anomalies Relative to MERRA-2

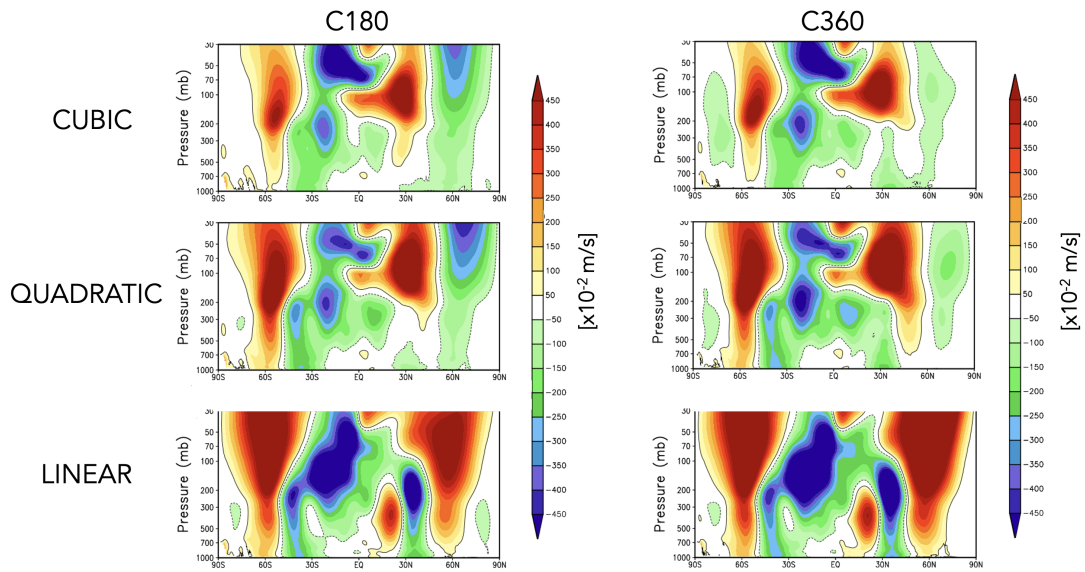


Figure 13. Colors shown anomalies in the DJF 1985-2015 climatological mean zonal mean zonal winds in the CUBIC (top), QUADRATIC (middle) and LINEAR (bottom) experiments, relative to MERRA-2. Results for both C180 (left) and C360 (right) experiments are shown.

DJF Climatological 30 hPa Zonal Wind Anomalies Relative to MERRA-2

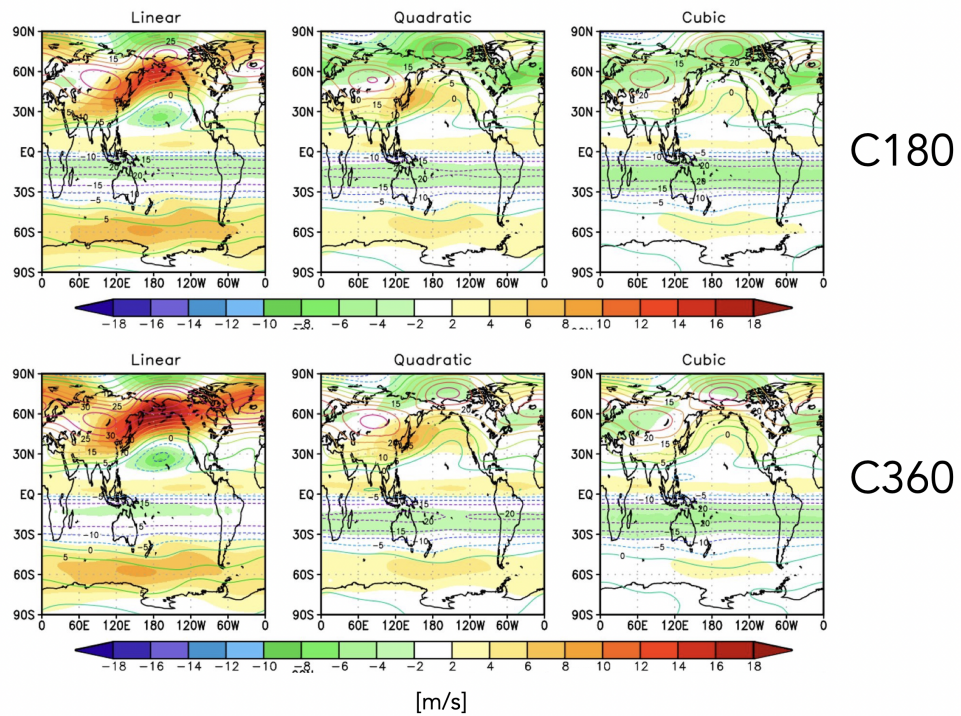


Figure 14. Colors shown anomalies in the DJF 1985-2015 climatological mean zonal winds at 30 hPa in the CUBIC (right), QUADRATIC (middle) and LINEAR (left) experiments, relative to MERRA-2. Results for both C180 (top) and C360 (bottom) experiments are shown.

591 #1. The stratospheric mean age-of-air in GEOS is sensitive to the degree of the
 592 interpolation scheme that is used to calculate layer-mean values of total energy, U, V and
 593 tracers. Different treatment of the vertical remapping algorithm result in mid-stratospheric
 594 (50 hPa) age-of-air differences of ~ 1 year over high latitudes, or about 30% climatolog-
 595 ical mean values.

596 #2. The increased age-of-air biases in more recent GEOS configurations are reflected
 597 in the increased biases in simulated trace gases, including CH₄ and N₂O.

598 #3. The age-of-air sensitivities reflect, to first order, changes in the strength of trop-
 599 ical upwelling associated with the Brewer-Dobson circulation which are in turn are driven
 600 by changes in EP flux convergence over northern midlatitudes. Changes in wave conver-
 601 gence reflect shifts in (critical lines of) wave propagation that originate in the troposphere
 602 over the Pacific Ocean, a region of strong upward wave activity.

603 #4. The degradation of upwelling statistics manifest in AMIPs, also translate to
 604 degradations in configurations of GEOS in which the meteorological fields are constrained
 605 or “replayed” to MERRA-2.

606 An important caveat should be mentioned in relation to Conclusion 3 listed above,
 607 which highlights the leading role played by *extratropical* wave convergences in the be-
 608 havior of tropical upwelling in the model. While this is consistent with our understand-
 609 ing that the Brewer-Dobson Circulation is, to first order, determined by extratropical
 610 wave flux convergences, in practice this means that other undesirable biases may emerge
 611 in the tropics (i.e., tropical temperatures, Figure 8). Our analysis of the M2AMIP en-
 612 semble, however, suggests that this tropical temperature bias is not a necessary conse-
 613 quence of the GMAO FV remapping scheme but, rather, emerges in tandem with other
 614 changes that were made in the model. Nonetheless, Figure 8 suggests that improvements
 615 in transport associated with the GMAO remapping scheme must be carefully weighed
 616 in the broader context of other model development choices.

617 Interestingly, preliminary analysis suggests that our findings may also translate to
 618 replay configurations of GEOS (Figure 10), although the effect is muted, relative to free-
 619 running configurations. As a rigorous evaluation of the stratospheric circulation in re-
 620 play and DAS configurations is beyond the scope of the current study, future work will
 621 therefore focus on assessing the extent to which the free-running model biases reported
 622 here are expressed when the model is run in data assimilation mode. It also bears em-
 623 phasizing that our findings do have immediate implications for the (free-running) sub-
 624 seasonal forecast and coupled chemistry climate applications of the GEOS model cur-
 625 rently in operation.

626 In addition to its implications for GEOS, our results more generally highlight the
 627 key role played by model numerics in transport (e.g., Rood (1987)). The sensitivities in
 628 the age-of-air documented herein are also consistent in spirit with the findings in Gupta
 629 et al. (2020) who showed significant age differences occurring between spectral versus
 630 finite-volume numerics. Our results, however, suggest that there remain large sensitiv-
 631 ities even within a given (FV) dynamical core.

632 Looking forward, our findings support and build on the recommendation proposed
 633 in Gupta et al. (2020) for the construction of dynamical core benchmark tests aimed at
 634 determining how underlying AGCM numerics impact climatological transport proper-
 635 ties. In particular, in addition to the age-of-air, the authors propose a range of strato-
 636 spheric circulation diagnostics that should be evaluated including the zonal mean zonal
 637 winds, eddy temperature variance and zonal spectra of eddy kinetic energy. Our anal-
 638 ysis reveals an important role to be played by the climatological zonal mean wind struc-
 639 ture as it impacts wave convergence over midlatitudes; we therefore also recommend ex-
 640 plicit consideration of the Eliassen Palm flux convergence and tropical upwelling (w^*)
 641 fields as they may be crucial for interpreting age-of-air changes.

642 One somewhat incidental – but practical - result from our analysis is that the statis-
643 tics of $\nabla \cdot \mathbf{F}$ and w^* are well approximated by ensembles of so-called EMIP integrations.
644 As these are substantially easier to run than AMIPs these could provide a “first pass”
645 when evaluating new proposed model development changes, without the immediate need
646 to integrate AMIP-style experiments. We emphasize, however, that this statement should
647 only apply to a first stage in model development as the age-of-air will reflect the time
648 integrated impacts of both advection and mixing.

649 Finally, we conclude by noting that, while we have focused on sensitivities within
650 the FV remapping algorithm, our results have highlighted important sensitivities to changes
651 in radiation and, to a lesser extent, changes in parameterized convection. Though not
652 the dominant drivers of the age-of-air changes identified here, the former could poten-
653 tially influence the age both directly through changes in thermal structure and indirectly
654 by modifying wave propagation and/or generation in the troposphere.

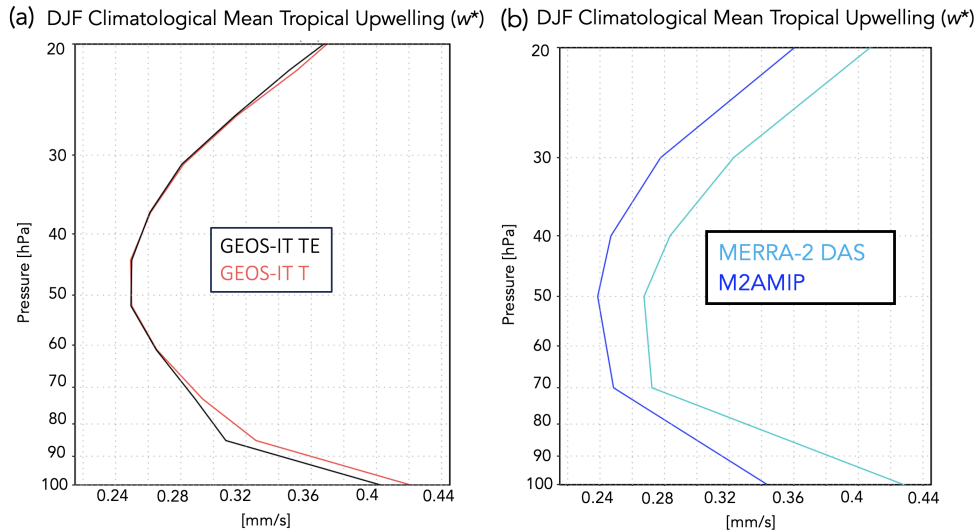


Figure A1. The DJF 1985–2015 climatological mean vertical residual mean velocity, w^* , averaged at each level between the turnaround latitudes compared between two experiments remapping to temperature (T) (red) versus total energy (TE) (black) (a) and between MERRA-2 DAS (cyan) and the M2AMIP ensemble (blue) (b). The underlying model code is consistent with the Version 5.29.4 GEOS-IT model.

655 Appendix A Sensitivities in Calculation of TEM Upwelling

656 There are various aspects of the calculation of the TEM circulation that warrant
 657 further comment. First, whereas the modeling experiments listed in Table 2 (rows 5–7)
 658 focus on the sensitivity of Step 5 within the GMAO FV core remapping algorithm to the
 659 choice of interpolation scheme, another difference between the GMAO and FV3 core remap-
 660 ping approaches is the use of TE versus T, respectively. To test the impact of this dif-
 661 ference, we ran a new experiment which is identical to the CUBIC experiment (Table
 662 2, row 7), except that T is remapped from input layer mean pressure locations to stan-
 663 dard output layer mean locations directly using cubic interpolation (i.e., no computa-
 664 tion of TE or a-posteriori energy conservation applied). Appendix Figure A1a shows that
 665 this has little impact on the strength of tropical upwelling, suggesting that the w^* dif-
 666 ferences associated with changes in the remapping algorithm are dominated by sensitiv-
 667 ities to the choice of interpolation scheme, not the use of TE versus T.

668 Second, the vertical component of the TEM circulation (w^*) shows some differences
 669 in vertical structure between MERRA-2 and the 30-member M2AMIP ensemble (Ap-
 670 pendix Figure A1b). This difference in vertical structure appears to reflect a difference
 671 between DAS and free-running configurations of the model, since other DAS configura-
 672 tions share a similar vertical structure (not shown). Given this difference, we ensure as
 673 apples-to-apples a comparison of simulated TEM velocities by comparing all AMIP re-
 674 sults to other AMIP experiments.

675 Appendix B Correspondence between EMIP and AMIP Upwelling

676 Appendix Figure B1 shows the close correspondence in DJF climatological mean
 677 w^* , averaged at each level between the turnaround latitudes, from AMIP and EMIP ex-

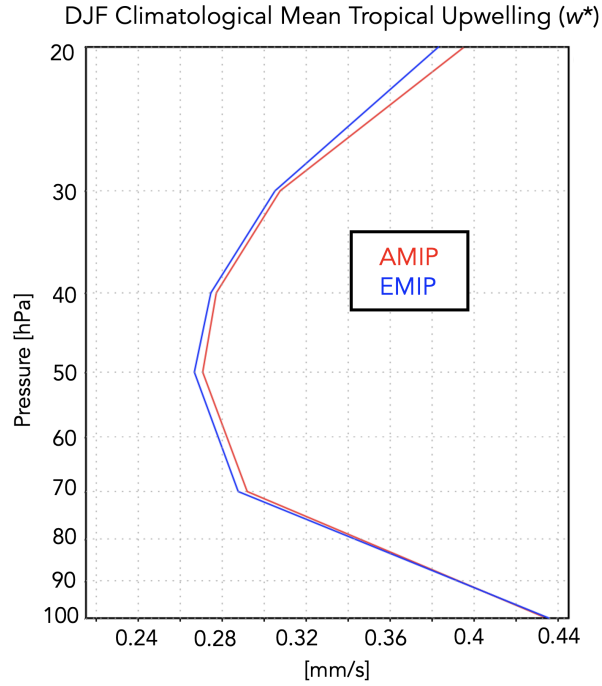


Figure B1. The DJF 1985-2015 climatological mean vertical residual mean velocity, w^* , averaged at each level between the turnaround latitudes for the CTRL experiment (Table 2, row 1). Results based on a 30-year-long AMIP experiment (red line) and a 30-member ensemble of three-month-long EMIP experiments (blue line) are shown.

678 periments using the same model configuration. This good agreement in upwelling is used
 679 to justify the analysis of the EMIP experiments listed in Table 2 (rows 5-7).

680 Appendix C Changes in Tropical and High Latitude Upwelling

681 Appendix Figure C1 compares the behavior in residual mean upwelling among the
 682 LINEAR, QUADRATIC and CUBIC experiments over the latitudes between the (tropi-
 683 cal) turnaround latitudes (left) and poleward of the northern turnaround latitude (right).
 684 The ordering among experiments in both regions reflects how increases in downwelling
 685 at high latitudes are, through mass balance, accompanied by enhanced upwelling in the
 686 tropics.

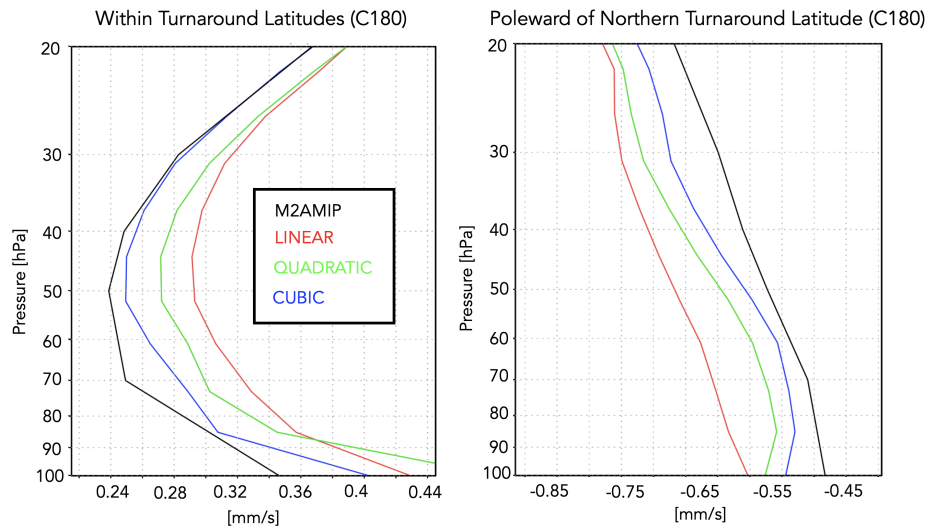
DJF Climatological Mean Upwelling (w^*)

Figure C1. Left: The DJF 1985-2015 climatological mean vertical residual mean velocity, w^* , averaged at each level between the turnaround latitudes for the LINEAR (red line; Table 2, row 5), QUADRATIC (green line; Table 2, row 6) and CUBIC (blue line; Table 2, row 7) experiments. M2AMIP is shown in black. Right: As in left panel, except averaged over latitudes poleward of the northern turnaround latitude. Results in both panels are shown for C180 experiments.

687

Appendix D Tropopause Pressure

688

Appendix Figure D1 compares boreal winter tropopause pressure and temperature among the LINEAR, QUADRATIC and CUBIC experiments, relative to MERRA-2.

689

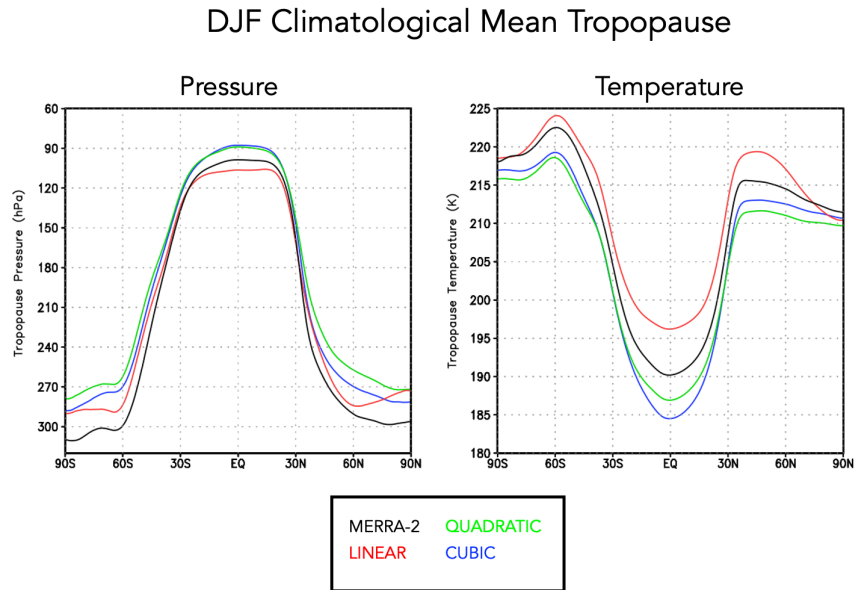


Figure D1. The DJF 1985-2015 climatological mean tropopause pressure (left) and temperature (right) in the CUBIC (blue), QUADRATIC (green) and LINEAR (red) experiments. MERRA-2 is shown in black. Results are shown for the C180 experiments.

690 Acronyms

- 691 **AMIP** Atmospheric Model Intercomparison Project
692 **CH₄** methane
693 **CCMs** chemistry climate models
694 **CCMI** Chemistry Climate Modeling Initiative
695 **CCMVal** Chemistry Climate Model Validation
696 **CO₂** carbon dioxide
697 **CTRL** control
698 **CTM** chemistry transport model
699 **DAS** Data assimilation
700 **DJF** December-January-February
701 **EMIP** ensemble AMIP
702 **EOS** Earth Observing System
703 **EP** Eliassen-Palm
704 **FV** finite-volume
705 **FP** Forward Processing
706 **GEOS** Global Earth Observing System
707 **GEOS-R21C** GEOS Retrospective analysis for the 21st Century
708 **GMI** Global Modeling Initiative
709 **HALOE** Halogen Occultation Experiment
710 **MERRA-2** Modern-Era Retrospective Analysis for Research and Applications v2
711 **MLS** Microwave Limb Sounder
712 **N₂O** nitrous oxide
713 **NH** northern hemisphere
714 **PPM** piecewise parabolic
715 **RRTMG** Rapid Radiative Transfer Model for GCMS

716 **SW** shortwave
 717 **TE** total energy
 718 **TEM** Transformed Eulerian Mean
 719 **UARS** Upper Atmosphere Research Satellite

720 **Open Research Section**

721 TBD

722 **Acknowledgments**

723 C.O. thanks Lawrence Coy for his insight which helped in interpreting the results and
 724 guiding experimental design. The authors also thank the high-performance computing
 725 resources provided by NASA’s Advanced Supercomputing (NAS) Division and the NASA
 726 Center for Climate Simulation (NCCS) as well as NASA’s Modeling, Analysis and Pre-
 727 diction (MAP) program, which supports the Global Modeling Assimilation Office and
 728 core chemistry-climate and chemistry-modeling activities.

729 **References**

- 730 Abalos, M., Calvo, N., Benito-Barca, S., Garny, H., Hardiman, S. C., Lin, P., ...
 731 others (2021). The Brewer–Dobson circulation in CMIP6. *Atmospheric*
 732 *Chemistry and Physics*, *21*(17), 13571–13591.
- 733 Abalos, M., Orbe, C., Kinnison, D. E., Plummer, D., Oman, L. D., Jöckel, P., ...
 734 others (2020). Future trends in stratosphere-to-troposphere transport in CCM1
 735 models. *Atmospheric Chemistry and Physics*, *20*(11), 6883–6901.
- 736 Abalos, M., Randel, W. J., Kinnison, D. E., & Garcia, R. R. (2017). Using the
 737 artificial tracer e90 to examine present and future UTLS tracer transport in
 738 WACCM. *Journal of the Atmospheric Sciences*, *74*(10), 3383–3403.
- 739 Andrews, D., Holton, J., & Leovy, C. (1987). Middle Atmosphere Dynam-
 740 ics. *Academic Press*, *60*, 489. doi: 10.1175/1520-0469(2003)060<0103:
 741 CEOOAL>2.0.CO;2
- 742 Boering, K. A., Wofsy, S., Daube, B., Schneider, H., Loewenstein, M., Podolske, J.,
 743 & Conway, T. (1996). Stratospheric mean ages and transport rates from obser-
 744 vations of carbon dioxide and nitrous oxide. *Science*, *274*(5291), 1340–1343.
- 745 Butchart, N., Cionni, I., Eyring, V., Shepherd, T., Waugh, D., Akiyoshi, H., ...
 746 others (2010). Chemistry–climate model simulations of twenty-first century
 747 stratospheric climate and circulation changes. *Journal of Climate*, *23*(20),
 748 5349–5374.
- 749 Chiodo, G., & Polvani, L. M. (2019). The response of the ozone layer to quadru-
 750 pled CO₂ concentrations: Implications for climate. *Journal of Climate*, *32*(22),
 751 7629–7642.
- 752 Chou, M.-D. (1990). Parameterizations for the absorption of solar radiation by O₂
 753 and CO₂ with application to climate studies. *Journal of Climate*, *3*(2), 209–
 754 217.
- 755 Chou, M.-D. (1992). A solar radiation model for use in climate studies. *Journal of*
 756 *Atmospheric Sciences*, *49*(9), 762–772.
- 757 Chou, M.-D., & Suarez, M. J. (1994). An efficient thermal infrared radiation param-
 758 eterization for use in general circulation models.
- 759 Collow, A. B. M., Mahanama, S. P., Bosilovich, M. G., Koster, R. D., & Schubert,
 760 S. D. (2017). *An evaluation of teleconnections over the united states in an*
 761 *ensemble of AMIP simulations with the MERRA-2 configuration of the GEOS*
 762 *atmospheric model* (Tech. Rep.).
- 763 Davis, N. A., Callaghan, P., Simpson, I. R., & Tilmes, S. (2022). Specified dynamics

- 764 scheme impacts on wave-mean flow dynamics, convection, and tracer transport
 765 in CESM2 (WACCM6). *Atmospheric Chemistry and Physics*, 22(1), 197–214.
- 766 Dietmüller, S., Eichinger, R., Garny, H., Birner, T., Boenisch, H., Pitari, G., ...
 767 others (2018). Quantifying the effect of mixing on the mean age of air in
 768 CCMVal-2 and CCM1-1 models. *Atmospheric Chemistry and Physics*, 18(9),
 769 6699–6720.
- 770 Eichinger, R., Garny, H., Šácha, P., Danker, J., Dietmüller, S., & Oberländer-Hayn,
 771 S. (2020). Effects of missing gravity waves on stratospheric dynamics: Part 1,
 772 Climatology. *Climate Dynamics*, 54(5), 3165–3183.
- 773 Eluszkiewicz, J., Hemler, R. S., Mahlman, J. D., Bruhwiler, L., & Takacs, L. L.
 774 (2000). Sensitivity of age-of-air calculations to the choice of advection scheme.
 775 *Journal of the Atmospheric Sciences*, 57(19), 3185–3201.
- 776 Eyring, V., Lamarque, J.-F., Hess, P., Arfeuille, F., Bowman, K., Chipperfield,
 777 M. P., ... others (2013). Overview of IGAC/SPARC Chemistry-Climate
 778 Model Initiative (CCMI) community simulations in support of upcoming ozone
 779 and climate assessments. *SPARC Newsletter*, 40(January), 48–66.
- 780 Freitas, S. R., Grell, G. A., Molod, A., Thompson, M. A., Putman, W. M., Santos e
 781 Silva, C. M., & Souza, E. P. (2018). Assessing the Grell-Freitas convection
 782 parameterization in the NASA GEOS modeling system. *Journal of Advances
 783 in Modeling Earth Systems*, 10(6), 1266–1289.
- 784 Gelaro, R., McCarty, W., Suárez, M. J., Todling, R., Molod, A., Takacs, L., ...
 785 others (2017). The modern-era retrospective analysis for research and applica-
 786 tions, version 2 (MERRA-2). *Journal of Climate*, 30(14), 5419–5454.
- 787 Grell, G. A., & Freitas, S. R. (2014). A scale and aerosol aware stochastic convective
 788 parameterization for weather and air quality modeling. *Atmospheric Chemistry
 789 and Physics*, 14(10), 5233–5250.
- 790 Groöb, J.-U., & Russell III, J. M. (2005). A stratospheric climatology for O₃, H₂O,
 791 CH₄, NO_x, HCl and HF derived from HALOE measurements. *Atmospheric
 792 Chemistry and Physics*, 5(10), 2797–2807.
- 793 Gupta, A., Gerber, E. P., & Lauritzen, P. H. (2020). Numerical impacts on tracer
 794 transport: A proposed intercomparison test of Atmospheric General Circula-
 795 tion Models. *Quarterly Journal of the Royal Meteorological Society*, 146(733),
 796 3937–3964.
- 797 Hall, T. M., & Plumb, R. A. (1994). Age as a diagnostic of stratospheric transport.
 798 *Journal of Geophysical Research: Atmospheres*, 99(D1), 1059–1070.
- 799 Hall, T. M., Waugh, D. W., Boering, K. A., & Plumb, R. A. (1999). Evaluation
 800 of transport in stratospheric models. *Journal of Geophysical Research: Atmo-
 801 spheres*, 104(D15), 18815–18839.
- 802 Hardiman, S. C., Butchart, N., & Calvo, N. (2014). The morphology of the Brewer-
 803 Dobson circulation and its response to climate change in CMIP5 simulations.
 804 *Quarterly Journal of the Royal Meteorological Society*, 140(683), 1958–1965.
- 805 Haynes, P., McIntyre, M., Shepherd, T., Marks, C., & Shine, K. P. (1991). On the
 806 “downward control” of extratropical diabatic circulations by eddy-induced
 807 mean zonal forces. *Journal of the Atmospheric Sciences*, 48(4), 651–678.
- 808 Hegglin, M. I., Brunner, D., Peter, T., Hoor, P., Fischer, H., Staehelin, J., ... Weers,
 809 U. (2006). Measurements of NO, NO_y, N₂O, and O₃ during SPURT: implica-
 810 tions for transport and chemistry in the lowermost stratosphere. *Atmospheric
 811 Chemistry and Physics*, 6(5), 1331–1350.
- 812 Holton, J. R., Haynes, P. H., McIntyre, M. E., Douglass, A. R., Rood, R. B., & Pfis-
 813 ter, L. (1995). Stratosphere-troposphere exchange. *Reviews of Geophysics*,
 814 33(4), 403–439.
- 815 Holzer, M., & Hall, T. M. (2000). Transit-time and tracer-age distributions in geo-
 816 physical flows. *Journal of the atmospheric sciences*, 57(21), 3539–3558.
- 817 Iacono, M. J., Delamere, J. S., Mlawer, E. J., Shephard, M. W., Clough, S. A., &
 818 Collins, W. D. (2008). Radiative forcing by long-lived greenhouse gases: Cal-

- 819 culations with the AER radiative transfer models. *Journal of Geophysical*
820 *Research: Atmospheres*, 113(D13).
- 821 Ivy, D. J., Solomon, S., Calvo, N., & Thompson, D. W. (2017). Observed connec-
822 tions of arctic stratospheric ozone extremes to Northern Hemisphere surface
823 climate. *Environmental Research Letters*, 12(2), 024004.
- 824 Kouatchou, J., Molod, A., Nielsen, J., Auer, B., Putman, W., & Clune, T. (2015).
825 *GEOS-5 chemistry transport model user's guide* (Tech. Rep.).
- 826 Legras, B., Pissot, I., Berthet, G., & Lefevre, F. (2004). Variability of the lagrangian
827 turbulent diffusivity in the lower stratosphere. *Atmospheric Chemistry and*
828 *Physics Discussions*, 4(6), 8285–8325.
- 829 Lin, S.-J. (2004). A “vertically lagrangian” finite-volume dynamical core for global
830 models. *Monthly Weather Review*, 132(10), 2293–2307.
- 831 Lin, S.-J., Putman, W., & Harris, L. (2017). *The gfdl finite-volume cubed-sphere dy-*
832 *namical core*. NWS/NCEP/EMC.
- 833 Molod, A., Takacs, L., Suarez, M., & Bacmeister, J. (2015). Development of the
834 GEOS-5 atmospheric general circulation model: Evolution from MERRA to
835 MERRA2. *Geoscientific Model Development*, 8(5), 1339–1356.
- 836 Monge-Sanz, B., Chipperfield, M., Simmons, A., & Uppala, S. (2007). Mean age of
837 air and transport in a CTM: Comparison of different ECMWF analyses. *Geo-*
838 *physical Research Letters*, 34(4).
- 839 Monge-Sanz, B. M., Bozzo, A., Byrne, N., Chipperfield, M. P., Diamantakis, M.,
840 Flemming, J., ... others (2022). A stratospheric prognostic ozone for seam-
841 less Earth system models: performance, impacts and future. *Atmospheric*
842 *Chemistry and Physics*, 22(7), 4277–4302.
- 843 Morgenstern, O., & Carver, G. D. (2001). Comparison of cross-tropopause transport
844 and ozone in the upper troposphere and lower stratosphere region. *Journal of*
845 *Geophysical Research: Atmospheres*, 106(D10), 10205–10221.
- 846 Neu, J., Strahan, S., Braesicke, P., Douglass, A., Huck, P., Oman, L., ... Tegtmeier,
847 S. (2010). SPARC CCMVal (2010), SPARC Report on the Evaluation of
848 Chemistry-Climate Models: Chapter 5: Transport. SPARC.
- 849 Neu, J. L., & Plumb, R. A. (1999). Age of air in a “leaky pipe” model of strato-
850 spheric transport. *Journal of Geophysical Research: Atmospheres*, 104(D16),
851 19243–19255.
- 852 Oehrlein, J., Chiodo, G., & Polvani, L. M. (2020). The effect of interactive ozone
853 chemistry on weak and strong stratospheric polar vortex events. *Atmospheric*
854 *Chemistry and Physics*, 20(17), 10531–10544.
- 855 Orbe, C., Oman, L. D., Strahan, S. E., Waugh, D. W., Pawson, S., Takacs, L. L., &
856 Molod, A. M. (2017). Large-scale atmospheric transport in GEOS replay simu-
857 lations. *Journal of Advances in Modeling Earth Systems*, 9(7), 2545–2560.
- 858 Orbe, C., Rind, D., Jonas, J., Nazarenko, L., Faluvegi, G., Murray, L. T., ... oth-
859 ers (2020). GISS Model E2.2: A climate model optimized for the middle
860 atmosphere—2. Validation of large-scale transport and evaluation of cli-
861 mate response. *Journal of Geophysical Research: Atmospheres*, 125(24),
862 e2020JD033151.
- 863 Orbe, C., Yang, H., Waugh, D. W., Zeng, G., Morgenstern, O., Kinnison, D. E., ...
864 others (2018). Large-scale tropospheric transport in the Chemistry–Climate
865 Model Initiative (CCMI) simulations. *Atmospheric Chemistry and Physics*,
866 18(10), 7217–7235.
- 867 Pan, L. L., Wei, J., Kinnison, D., Garcia, R., Wuebbles, D., & Brasseur, G. P.
868 (2007). A set of diagnostics for evaluating chemistry-climate models in the ex-
869 tratropical tropopause region. *Journal of Geophysical Research: Atmospheres*,
870 112(D9).
- 871 Pawson, S., Stajner, I., Kawa, S. R., Hayashi, H., Tan, W.-W., Nielsen, J. E., ...
872 Livesey, N. J. (2007). Stratospheric transport using 6-h-averaged winds from
873 a data assimilation system. *Journal of Geophysical Research: Atmospheres*,

- 874 112(D23).
- 875 Plumb, R. A. (1985). On the three-dimensional propagation of stationary waves.
876 *Journal of Atmospheric Sciences*, 42(3), 217–229.
- 877 Plumb, R. A. (1996). A “tropical pipe” model of stratospheric transport. *Journal of*
878 *Geophysical Research: Atmospheres*, 101(D2), 3957–3972.
- 879 Plumb, R. A. (2002). Stratospheric transport. *Journal of the Meteorological Society*
880 *of Japan. Ser. II*, 80(4B), 793–809.
- 881 Polvani, L. M., Waugh, D. W., Correa, G. J., & Son, S.-W. (2011). Stratospheric
882 ozone depletion: The main driver of twentieth-century atmospheric circulation
883 changes in the southern hemisphere. *Journal of Climate*, 24(3), 795–812.
- 884 Prather, M. J., Zhu, X., Tang, Q., Hsu, J., & Neu, J. L. (2011). An atmospheric
885 chemist in search of the tropopause. *Journal of Geophysical Research: Atmo-*
886 *spheres*, 116(D4).
- 887 Rood, R. B. (1987). Numerical advection algorithms and their role in atmospheric
888 transport and chemistry models. *Reviews of geophysics*, 25(1), 71–100.
- 889 Rosenlof, K. H. (1995). Seasonal cycle of the residual mean meridional circulation
890 in the stratosphere. *Journal of Geophysical Research: Atmospheres*, 100(D3),
891 5173–5191.
- 892 Son, S.-W., Tandon, N. F., Polvani, L. M., & Waugh, D. W. (2009). Ozone hole and
893 Southern Hemisphere climate change. *Geophysical Research Letters*, 36(15).
- 894 Strahan, S., Douglass, A., & Newman, P. (2013). The contributions of chemistry
895 and transport to low arctic ozone in March 2011 derived from aura MLS obser-
896 vations. *Journal of Geophysical Research: Atmospheres*, 118(3), 1563–1576.
- 897 Thiele, G., & Sarmiento, J. (1990). Tracer dating and ocean ventilation. *Journal of*
898 *Geophysical Research: Oceans*, 95(C6), 9377–9391.
- 899 Waugh, D., & Hall, T. (2002). Age of stratospheric air: Theory, observations, and
900 models. *Reviews of Geophysics*, 40(4), 1–1.
- 901 Weaver, C. J., Douglass, A. R., & Rood, R. B. (1993). Thermodynamic balance
902 of three-dimensional stratospheric winds derived from a data assimilation
903 procedure. *Journal of Atmospheric Sciences*, 50(17), 2987–2993.